
The Effects of Large-Scale Magnetic Fields on Disk Formation and Evolution

Arieh Königl¹ and Raquel Salmeron²

¹ Department of Astronomy & Astrophysics, The University of Chicago, Chicago IL 60637, USA akonigl@uchicago.edu

² Research School of Astronomy & Astrophysics and Research School of Earth Sciences, The Australian National University, Canberra ACT 0200, Australia raquel@mso.anu.edu.au

1 Introduction

In Chap. V [Magnetohydrodynamics of Protostellar Disks] it was shown that a sufficiently highly conducting Keplerian disk that is threaded by a weak magnetic field will be subject to the magnetorotational instability (MRI) and may evolve into a turbulent state in which the field is strongly amplified and has a *small-scale, disordered* configuration. This turbulence has been proposed as the origin of the effective viscosity that enables matter to accrete by transferring angular momentum *radially* out along the disk plane. In this chapter we focus on an alternative mode of angular momentum transport that can play an important role in protostellar disks, namely, *vertical* transport through the disk surfaces effected by the stresses of a *large-scale, ordered* magnetic field that threads the disk.

The possible existence of a comparatively strong, “open” magnetic field over much of the extent of at least some circumstellar disks around low- and intermediate-mass protostars is indicated by far-IR and submillimeter polarization measurements, which have discovered an ordered, hourglass-shaped field morphology on sub-parsec scales in several molecular clouds (e.g., Schleuning 1998; Girart et al. 2006; Kirby 2009). The polarized radiation is attributed to thermal emission by spinning dust grains whose short axes are aligned along the magnetic field (e.g., Lazarian 2007). The detected hourglass morphology arises naturally in molecular cloud cores in which a large-scale magnetic field provides dynamical support against the core’s self-gravity (see Sect. 2.1). In this picture the field is *interstellar* in origin and is part of the Galactic magnetic field distribution. As discussed in Sect. 3, the inward gravitational force can become dominant and the core then undergoes dynamical collapse to form a central protostar and a circumstellar disk. The magnetic field is dragged in by the infalling matter and could in principle lead to a large-scale “open” field configuration in the disk.

An ordered magnetic field that threads a disk can exert a magnetic torque that removes angular momentum from the interior gas. This angular momentum can be carried away along the field lines either by *torsional Alfvén waves* in a process known as magnetic braking (see Sect. 2.2) or through a rotating outflow in what is known as a *centrifugally driven wind* (CDW; see Sect. 4.3). These mechanisms could supplement or even entirely supplant the radial transport along the disk plane invoked in traditional disk models: by turbulent stresses as in the MRI scenario mentioned above or through gravitational torques in a self-gravitating disk as described in Chap. IV [Disk Hydrodynamics]. In the case of radial transport, the angular momentum removed from the bulk of the matter is deposited into a small amount of gas at the outer edge of the disk. In the case of vertical transport, this angular momentum is deposited into a small fraction of the disk mass (the tenuous surface layers of the disk) that is removed as a CDW or else (when magnetic braking operates) into the ambient medium through which the torsional Alfvén waves propagate. The introduction of this new transport channel has profound implications to the structure and properties of disks in which it is a major contributor to the angular momentum budget and potentially also to the strong connection that has been found between accretion and outflow phenomena in young stellar objects. This is discussed in Sect. 4, where we also consider how to determine which of the two possible angular momentum transport modes (radial or vertical) operates at any given location in a magnetically threaded disk and whether these two modes can coexist.

Of course, large-scale, ordered magnetic fields can also be produced *in situ* by a *dynamo* process; we consider this alternative possibility for the origin of the disk field in Sect. 4.2. In the case of the Sun, high-resolution observations made at extreme ultraviolet and soft X-ray wavelengths and transformed into spectacular false-color images have revealed a complex web of organized structures that appear as loops and prominences near the stellar surface but simplify to a more uniform distribution further out (e.g., Balogh et al. 1995). There is growing evidence that Sun-like stars are already magnetically active in the protostellar phase and, in fact, generate fields that are a thousand times stronger than that of the present-day Sun. The dynamical interaction between such a field and a surrounding accretion disk through which mass is being fed to the nascent star could have important evolutionary and observational consequences. We consider this in Sect. 5. We conclude with a summary and a discussion of future research directions in Sect. 6.

2 MHD of Magnetically Threaded Disks

Before getting into the specifics of the various topics outlined in Sect. 1, we present a general discussion of the dynamical properties of ordered magnetic fields in relation to protostellar disks and of the main methods that have been applied to their study.

2.1 Magnetic Forces

The magnetic force per unit volume on a magnetized fluid element is given by

$$\frac{\mathbf{J} \times \mathbf{B}}{c} = -\nabla \left(\frac{B^2}{8\pi} \right) + \frac{\mathbf{B} \cdot \nabla \mathbf{B}}{4\pi}, \quad (1)$$

where \mathbf{J} is the current density, \mathbf{B} is the magnetic field vector, c is the speed of light, and we substituted

$$\mathbf{J} = \frac{c}{4\pi} \nabla \times \mathbf{B} \quad (2)$$

(neglecting the displacement current in Ampère’s Law on the assumption that all speeds are $\ll c$) and used a vector identity to obtain the two terms on the right-hand side of Eq. (1). As was already noted in Chap. V, the first term represents the magnetic pressure force and the second one the force due to magnetic tension. To build intuition it is useful to consider the magnetic *field lines*. Because of the solenoidal (i.e., absence of monopoles) condition on the magnetic field,

$$\nabla \cdot \mathbf{B} = 0, \quad (3)$$

the flux Ψ of “open” field lines through the disk (the integral $\int \mathbf{B} \cdot d\mathbf{S}$, where $d\mathbf{S}$ is a disk surface-area element) is conserved. This is a noteworthy result: it says that, even if the disk is resistive in its interior, the flux of magnetic field lines that thread it (also referred to as the *poloidal flux*) will not be destroyed (although poloidal flux could be added to, or removed from, the disk through its outer and inner boundaries). In the MHD picture, the field lines can be thought of as rubber bands that exert *tension* of magnitude $B^2/4\pi$ directed *along* the field and *pressure* of magnitude $B^2/8\pi$ *normal* to their local direction (e.g., Parker 1979).

The nonmagnetic forces acting on a cloud core or a disk are the force of gravity (mostly self-gravity in the case of a core and central-mass gravity in the case of a nearly Keplerian disk), $-\rho\nabla\Phi$ (where ρ is the mass density and Φ is the gravitational potential), and the thermal pressure force $-\nabla P$. There may be an additional force, associated with the momentum flux of MHD waves, in a turbulent system. Such turbulence could give rise to an effective viscosity, but, as is generally the case in astrophysical systems, the effects of microphysical shear viscosity would remain negligible (e.g., Frank et al. 2002). Protostellar disks typically have sufficiently low temperatures that the dominant forces in the disk plane are gravity and magnetic tension, whereas in the vertical direction the thermal pressure force is always important, balancing the downward force of gravity or of the magnetic pressure gradient.

These notions can be illustrated by considering the equilibrium configurations of cloud cores (e.g., Mouschovias 1976). Within the interstellar gas that ultimately ends up in the core the magnetic field lines are initially nearly parallel to each other and the field is well coupled to the matter (with the

magnetic flux being, in the jargon of MHD, “frozen” into the matter). Since a magnetic field exerts no force parallel to itself, matter can slide relatively easily along the field to form a flattened mass distribution. The oblate structure predicted by this scenario is consistent with the observed shapes of starless cores in the Orion giant molecular cloud (e.g., Tassis 2007).³ It is convenient to describe this configuration with the help of a cylindrical coordinate system $\{r, \phi, z\}$ centered on the forming star, with the z axis aligned with the initial magnetic field direction. A vertical hydrostatic equilibrium in which the (upward) thermal (and possibly turbulent) pressure force balances the (downward) gravitational force is established on a dynamical (free-fall) time scale and is by and large maintained throughout the subsequent evolution of the core, as verified by numerical simulations (e.g., Fiedler & Mouschovias 1993; Galli & Shu 1993), including in cases of filamentary clouds that are initially elongated in the field direction (e.g., Nakamura et al. 1995; Tomisaka 1996). Self-gravity acting in the radial direction tends to pull the field lines inward. The hourglass shape revealed by the polarization measurements is produced because these field lines remain anchored in the cloud envelope. This results in magnetic tension that is associated mainly with the term $(B_z/4\pi)dB_r/dz$ in Eq. (1) and is in complete analogy with the force exerted by a stretched rubber band. The field morphologies revealed by the polarization measurements are interpreted as arising from the approximate balance between this force and radial gravity. This interpretation is supported by H I and OH Zeeman measurements of the line-of-sight field amplitude and by estimates of the plane-of-sky field strength using the measured dispersion in the field orientation (the Chandrasekhar-Fermi method), both of which typically imply roughly virialized cores (with ordered and turbulent magnetic fields contributing approximately equally to the overall support of the cloud against self-gravity; e.g., Ward-Thompson et al. 2007).

In applying these ideas to the disks that form from the gravitational collapse of cores, one should bear in mind the following two points. First, the flux threading the disk is sufficiently strongly concentrated that the bending of the field lines between the midplane (where $B_r = B_\phi = 0$ by reflection symmetry) and the disk surface can be large enough to make $B_{r,s}$ (where the subscript ‘s’ denotes the surface) comparable to B_z (which, in turn, changes little between the midplane and the surface if the disk is thin). Consequently, *magnetic squeezing* by the z -gradient of the magnetic pressure associated with the B_r (and possibly also B_ϕ) field components can become comparable to, or even exceed, the downward force of gravity. This is indeed a key property of the wind-driving disk models discussed in Sect. 4.4. Second, the density scale height h in the disk typically satisfies $h \ll r$, implying a rapid decrease of the

³ Note, however, that many cores do not exhibit a clear oblate structure and that, in fact, many of the cores in Taurus are apparently prolate and may have formed from the fragmentation of the filamentary clouds in which they are embedded (e.g., Di Francesco et al. 2007).

density with z even as the magnetic field amplitude changes little for $z \lesssim r$. Therefore, magnetic forces generally dominate all other forces on scales $\gtrsim r$ above the disk surface, and the field there assumes a so-called “force-free” field configuration ($\mathbf{J} \times \mathbf{B} \approx 0$). According to Eq. (1), in this case the magnetic tension force has to balance the magnetic pressure force, which points outward (as B_z^2 increases toward the center). This implies that the field lines in this region assume a vase-like, “concave in” morphology (i.e., bending toward the vertical axis), in contradistinction to the hourglass-like, “convex out” shape that they have inside the disk. This behavior accounts for the initial collimation of disk-driven MHD winds (see Sect. 4.3).

2.2 Magnetic Braking

Plucked rubber bands (or strings) carry waves whose phase velocity is the square root of the ratio of the tension to the mass density. Using again the analogy to magnetic field lines, one immediately obtains the phase speed of (transverse) Alfvén waves, $v_{Az} = B_z/\sqrt{4\pi\rho}$ (taking the background field to point in the $\hat{\mathbf{z}}$ direction). When the transverse magnetic field of the wave points in the azimuthal direction, the corresponding (torsional) Alfvén wave carries angular momentum. A rotating molecular cloud core or disk will twist the magnetic “rubber bands” that thread it. The degree of twisting fixes the pitch $|B_{\phi,s}/B_z|$ of the field lines and is determined, in turn, by the “load” on the other end of the band (i.e., by the inertia of the external matter to which the field lines are coupled). This twisting represents a transfer of angular momentum from the core or disk to the external medium (subscript ‘ext’). One can thus determine $B_{\phi,s}$ by equating the torque per unit area (normal to $\hat{\mathbf{z}}$) exerted on each of the two surfaces of the flattened core or disk, $rB_zB_{\phi,s}/4\pi$, to minus the rate per unit area of angular momentum carried by the waves from each surface and deposited in the (initially nonrotating) ambient medium, $-\rho_{\text{ext}}r_{\text{ext}}^2\Omega_B v_{A\text{ext}}$, where Ω_B is the angular velocity of the field line (which is conserved along the field under ideal-MHD conditions; see Sect. 4.3). Poloidal flux conservation along the field makes it possible to relate the radius r and field B_z in the core or disk to the corresponding quantities in the external medium, $B_z r dr = B_{z,\text{ext}} r_{\text{ext}} dr_{\text{ext}}$, where the ambient field (assumed to be uniform on large scales) can be expressed in terms of the poloidal flux Ψ by $B_{z,\text{ext}} = \Psi/\pi r_{\text{ext}}^2$. One then obtains (cf. Basu & Mouschovias 1994)

$$B_{\phi,s} = -\frac{\Psi}{\pi r^2} \frac{v_{B\phi}}{v_{A\text{ext}}}, \quad (4)$$

where $v_{B\phi} = r\Omega_B$. The general meaning of $v_{B\phi}$ is discussed in Sect. 2.4; unless Ohm diffusivity dominates in the core/disk, it can be identified with the midplane angular velocity of the particles into which the field lines are frozen (see Eq. (65)).

2.3 Centrifugal Wind Driving

As noted in Sect. 2.1, the dynamics just above the disk surface is magnetically dominated, i.e., the magnetic energy density there is larger than the thermal, gravitational, and kinetic energy densities of the gas. The comparatively large electrical conductivity in this region implies that the poloidal (r, z) gas velocity is parallel to the poloidal magnetic field (see Sect. 4.3) and the bulk particle motions can be approximated as those of beads along rotating, rigid, massless wires (Henriksen & Rayburn 1971). This mechanical analogy is useful for deriving the criterion for the centrifugal launching of disk winds (Blandford & Payne 1982). We neglect thermal effects in this derivation and, correspondingly, regard the disk as being infinitely thin. Since the field geometry only varies on a scale $\sim r$ in the force-free zone, very close to the disk surface the field lines can be regarded as being nearly straight. Considering thus a straight wire that intersects a Keplerian disk at a distance r_0 from the center and makes an angle θ to the disk normal, the balance of gravitational and centrifugal forces *along* the wire implies that, in equilibrium, the effective potential $\Phi_{\text{eff}}(y)$ satisfies

$$\frac{\partial \Phi_{\text{eff}}}{\partial y} = \frac{y + \sin \theta}{(1 + 2y \sin \theta + y^2)^{3/2}} - y \sin^2 \theta - \sin \theta = 0, \quad (5)$$

where the dimensionless variable $y \equiv s/r_0$ measures the distance s along the wire. The equilibrium is unstable when $\partial^2 \Phi_{\text{eff}} / \partial y^2 < 0$ (corresponding to a local maximum of Φ_{eff}), which at $y = 0$ occurs for $\theta > 30^\circ$. Hence, centrifugal driving sets in if

$$\frac{B_{r,s}}{B_z} > \frac{1}{\sqrt{3}}. \quad (6)$$

This wind-launching criterion plays a key role in wind-driving disk models. It is worth noting that, in contrast to typical stellar winds, in which the outflowing gas must “climb out” of basically the entire gravitational potential well at the stellar surface, in the case of outflows from a rotationally supported, infinitely thin disk the depth of the (gravitational + centrifugal) potential well is lower by a factor of 2 on account of the rotation, and gas can in principle “escape to infinity” without any added thermal push if there is a sufficiently strongly inclined, rigid channel (the magnetic field lines). Real disks, however, are not completely cold and therefore have a finite thickness. When this is taken into account, the effective potential attains a maximum at some height above the disk surface, and thermal pressure forces are required to lift gas from the disk up to that point (e.g., Ogilvie 1997). This and some other properties of CDWs are considered in Sect. 4.3.

2.4 Nonideal MHD

Unlike the approach of classical electrodynamics, in which it is common to consider the magnetic field as being generated by current flows according to

the Biot-Savart law, in MHD practice it is often more illuminating to focus on the magnetic field and to regard the current density as a subordinate quantity that is determined, through Eq. (2), by how the field is shaped by its interaction with matter (e.g., Parker 2007). The current, in turn, helps to determine the neutral-fluid-frame (denoted by a prime) electric field \mathbf{E}' according to Ohm's law

$$\mathbf{J} = \sigma \cdot \mathbf{E}' = \sigma_{\text{O}} \mathbf{E}'_{\parallel} + \sigma_{\text{H}} \hat{\mathbf{B}} \times \mathbf{E}'_{\perp} + \sigma_{\text{P}} \mathbf{E}'_{\perp}, \quad (7)$$

where the conductivity has been expressed as a tensor to take account of the inherent anisotropy that an ordered magnetic field induces in the motions of charged particles. Here the subscripts \parallel and \perp denote vector components that are, respectively, parallel and perpendicular to the unit vector $\hat{\mathbf{B}}$, whereas σ_{O} , σ_{H} , and σ_{P} are, respectively, the Ohm, Hall, and Pedersen conductivity terms.

Under ideal-MHD conditions, the conductivity is effectively infinite and the comoving electric field vanishes. This is an adequate approximation for describing the dynamics of a disk wind or of the medium surrounding the core/disk. However, within the core or disk themselves the degree of ionization is generally low, so finite conductivity effects must be taken into account in the dynamical modeling. When the conductivity is low, each charged particle species (denoted by a subscript 'j') develops a drift velocity $\mathbf{v}_{\text{d},j} \equiv \mathbf{v}_j - \mathbf{v}$ with respect to the neutral fluid velocity (which we approximate by the average fluid velocity \mathbf{v} , as appropriate for a weakly ionized medium). The drift velocities can be calculated from the equations of motion of these species, each of which is well approximated by a steady-state balance between the Lorentz force and the drag force \mathbf{F}_{nj} exerted by collisions with the neutrals,

$$Z_j e \left(\mathbf{E}' + \frac{\mathbf{v}_{\text{d},j}}{c} \times \mathbf{B} \right) = -\mathbf{F}_{\text{nj}} = m_j \gamma_j \varrho \mathbf{v}_{\text{d},j}, \quad (8)$$

where Z_j is the (signed) particle charge in units of the electronic charge e , $\gamma_j \equiv \langle \sigma v \rangle_j / (m_j + m)$, and $\langle \sigma v \rangle_j$ is the rate coefficient for collisional momentum transfer between particles of mass m_j and neutrals (of mass m and mass density ϱ). This collisional interaction in turn exerts a force $\mathbf{F}_{\text{jn}} = -\mathbf{F}_{\text{nj}}$ on the neutrals. The degree of coupling between a given charged species and the magnetic field is measured by the *Hall parameter*, defined as the ratio of the particle's gyrofrequency to its collision frequency $\nu_{\text{jn}} = \gamma_j \varrho$ with the neutrals:

$$\beta_j \equiv \frac{|Z_j| e B}{m_j c} \frac{1}{\gamma_j \varrho}. \quad (9)$$

In this expression, $B \equiv |\mathbf{B}| \text{sgn}\{B_z\}$ is the *signed* magnetic field amplitude, with the sign introduced to keep the dependence of the Hall conductivity on the magnetic field polarity (see Eq. (13) below). When $|\beta_j| \gg 1$ the coupling is good and the collision term can be neglected in comparison with the magnetic term; in this case the Lorentz force is approximately zero, corresponding to

the near vanishing of the electric field in the charged particle's frame. On the other hand, when $|\beta_j| \ll 1$ the coupling is poor; in this case the magnetic term in Eq. (8) can be neglected.

By summing up Eq. (8) over the particle species one obtains

$$\sum_j n_j \mathbf{F}_{jn} = \frac{\mathbf{J} \times \mathbf{B}}{c}. \quad (10)$$

This shows explicitly that, in a weakly ionized medium, the Lorentz force (which acts only on the charged particles) is transmitted to the bulk of the matter only through a collisional drag, which involves a relative motion between the charged and neutral components. Therefore, if magnetic forces are important in such a medium, its structure is *inherently not static*. This is exemplified by the behavior of a magnetically supported molecular cloud core (e.g., Shu et al. 1987). The magnetic field that threads the core is anchored in the comparatively well-ionized cloud envelope, but in the core's interior the degree of ionization is low and the magnetic tension force is transmitted to the predominantly neutral gas through ion-neutral drag. Since the ions (taken in what follows to constitute a single species denoted by the subscript 'i') are well coupled to the magnetic field and thus remain nearly fixed in space, the associated *ambipolar diffusion* drift entails an inward motion of the neutral particles toward the center of mass. If the evolution lasts longer than the ambipolar diffusion time ($\sim (R/v_A)^2 \gamma_i \varrho_i$, which can be inferred from Eqs. (14) and (18) below), the central concentration will become large enough to cause the core to become gravitationally unstable, and dynamical collapse will ensue.

Expressing the current density in terms of the charged particles' drifts,

$$\mathbf{J} = \sum_j en_j Z_j \mathbf{v}_{d,j} \quad (11)$$

(where the charged particles have number densities n_j and satisfy charge neutrality, $\sum_j n_j Z_j = 0$), and using Eq. (8), one can solve for the conductivity tensor components in Eq. (7):

$$\sigma_O = \frac{ec}{B} \sum_j n_j |Z_j| \beta_j, \quad (12)$$

$$\sigma_H = \frac{ec}{B} \sum_j \frac{n_j |Z_j|}{1 + \beta_j^2}, \quad (13)$$

and

$$\sigma_P = \frac{ec}{B} \sum_j \frac{n_j |Z_j| \beta_j}{1 + \beta_j^2} \quad (14)$$

(e.g., Cowling 1976; Wardle & Ng 1999). Note that σ_H (and correspondingly the Hall term in Ohm's law) depends on an odd power of the magnetic field

amplitude and can therefore have either a positive or a negative sign (reflecting the magnetic field polarity). This leads to qualitative differences in the behavior of the disk solutions in the Hall regime for positive and negative values of B_z .

The conductivity tensor formalism is useful for constructing realistic disk models in which the relative magnitudes of the different conductivities can change as a function of height even at a single radial location as a result of the variation in the density and in the dominant ionization mechanism as one moves between the disk surface and the midplane (see Sect. 4.4). It is nevertheless instructive to relate this formalism to the classical diffusivity regimes considered in Chap. V. This is best done by solving for the fluid-frame electric field,

$$c\mathbf{E}' = \eta_{\text{O}}\nabla \times \mathbf{B} + \eta_{\text{H}}(\nabla \times \mathbf{B}) \times \hat{\mathbf{B}} + \eta_{\text{A}}(\nabla \times \mathbf{B})_{\perp}, \quad (15)$$

where the Ohm, Hall, and ambipolar diffusivities are given, respectively, by

$$\eta_{\text{O}} = \frac{c^2}{4\pi\sigma_{\text{O}}}, \quad (16)$$

$$\eta_{\text{H}} = \frac{c^2}{4\pi\sigma_{\perp}} \frac{\sigma_{\text{H}}}{\sigma_{\perp}}, \quad (17)$$

and

$$\eta_{\text{A}} = \frac{c^2}{4\pi\sigma_{\perp}} \frac{\sigma_{\text{P}}}{\sigma_{\perp}} - \eta_{\text{O}}, \quad (18)$$

with $\sigma_{\perp} \equiv (\sigma_{\text{H}}^2 + \sigma_{\text{P}}^2)^{1/2}$ (e.g., Mitchner & Kruger 1973; Nakano et al. 2002). The three distinct regimes are delineated by

$$\begin{array}{ll} \sigma_{\text{O}} \approx \sigma_{\text{P}} \gg |\sigma_{\text{H}}| & \text{Ohm} \\ \sigma_{\text{O}} \gg |\sigma_{\text{H}}| \gg \sigma_{\text{P}} & \text{Hall} \\ \sigma_{\text{O}} \gg \sigma_{\text{P}} \gg |\sigma_{\text{H}}| & \text{ambipolar .} \end{array} \quad (19)$$

When ions and electrons (subscript ‘e’) are the only charged species, one has $\eta_{\text{H}} = \beta_{\text{e}}\eta_{\text{O}}$ and $\eta_{\text{A}} = \beta_{\text{i}}\beta_{\text{e}}\eta_{\text{O}}$, with the respective Hall parameters given numerically by $\beta_{\text{i}} = q\beta_{\text{e}} \approx 0.46(B/n_{13})$ (e.g., Draine et al. 1983; where $q \approx 1.3 \times 10^{-3} T_2^{1/2}$, $n_{13} = n_{\text{H}}/(10^{13} \text{ cm}^{-3})$, B is measured in Gauss, $T_2 = T/(10^2 \text{ K})$, and the mean ion mass is $m_{\text{i}} = 30 m_{\text{H}}$). In this case the three classical regimes correspond, respectively, to the Hall parameter ranges $|\beta_{\text{i}}| \ll |\beta_{\text{e}}| \ll 1$ (Ohm), $|\beta_{\text{i}}| \ll 1 \ll |\beta_{\text{e}}|$ (Hall), and $1 \ll |\beta_{\text{i}}| \ll |\beta_{\text{e}}|$ (ambipolar).

Figure 1 shows the regions of ambipolar, Hall and Ohm dominance in the $\log n_{\text{H}} - \log B$ plane.⁴ Molecular cloud cores and the outer regions ($\gtrsim 10 \text{ AU}$) of protostellar disks typically correspond to the ambipolar regime, as do the

⁴ For a complementary figure in the $\log n_{\text{H}} - \log T$ plane, see Fig. 2 of Chap. V.

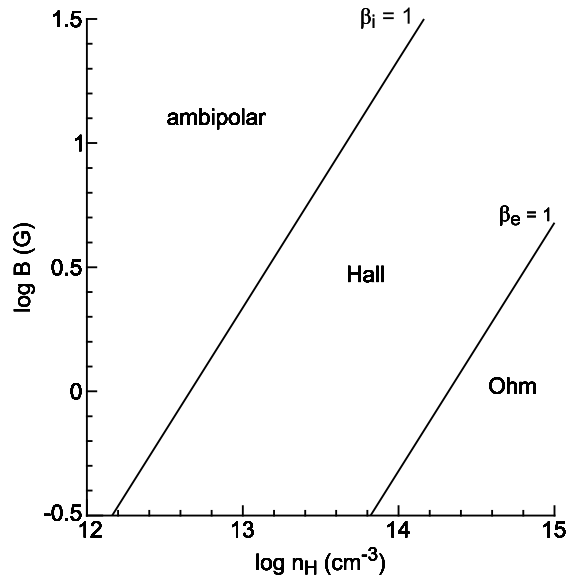


Fig. 1. Magnetic diffusivity regimes in the $\log n_{\text{H}} - \log B$ plane for $T = 280$ K.

disk surface regions at smaller radii; disk midplanes on scales $\sim 1 - 10$ AU are often dominated by Hall diffusivity, whereas Ohm diffusivity characterizes the midplanes of disks on scales $\sim 0.1 - 1$ AU. In the innermost ($\lesssim 0.1$ AU) regions of the disk, where the temperature increases above $\sim 10^3$ K and the gas becomes collisionally ionized (e.g., Gammie 1996; Li 1996a), anomalous Ohm diffusivity (the enhanced drag between positive and negative charge carriers due to scattering off electromagnetic waves generated by current-driven plasma instabilities) might play a role. Note that the precise extent of the different regimes depends on the radial profile of the disk column density, since the latter determines the degree of penetration of the ionizing radiation or cosmic rays (see Sect. 4.4). For a given mass accretion rate, the column density depends on the nature of the angular momentum transport mechanism. In particular, transport by a large-scale, ordered magnetic field is generally more efficient than transport by a small-scale, disordered field,⁵ resulting in higher inflow speeds and correspondingly lower column densities and higher degrees of ionization in CDW-mediated accretion than in MRI-based turbulent disks.

The behavior of the electric field is governed by Faraday's Law,

⁵ This can be seen by representing the $r\phi$ turbulent stress component as αP (where the constant α is typically < 1 ; cf. Balbus & Papaloizou 1999), so the ratio of the torques exerted by the ordered field and by the turbulent stress is $(-B_z B_{\phi,s}/4\pi\langle P\rangle)(r/\alpha H)$ (where $\langle \rangle$ denotes vertical averaging over the disk half-thickness H), which is typically $\gg 1$.

$$\frac{\partial \mathbf{B}}{\partial t} = -c \nabla \times \mathbf{E} , \quad (20)$$

where $\mathbf{E} = \mathbf{E}' - \mathbf{v} \times \mathbf{B}/c$ is the lab-frame electric field. In view of Eq. (15), when the resistive term in the expression for \mathbf{E}' can be neglected and the only charge carriers are ions and electrons, one can express the ambipolar and Hall contributions to $c\mathbf{E}$ as $(\mathbf{v} - \mathbf{v}_i) \times \mathbf{B}$ and $(\mathbf{v}_i - \mathbf{v}_e) \times \mathbf{B}$, respectively (see Königl 1989 and Chap. V), yielding $\partial \mathbf{B}/\partial t = \nabla \times (\mathbf{v}_e \times \mathbf{B})$, which indicates that in this case the field lines are frozen into the electrons (the particle species with the highest mobility $|Z_j|e/m_j$). It is also seen that the ideal-MHD limit $\mathbf{E} = -\mathbf{v} \times \mathbf{B}/c$ is approached when the ion-neutral and ion-electron drift speeds are small in comparison with the bulk speed. It further follows that, in the ambipolar regime, the ions and electrons drift together relative to the neutrals (i.e., $|\mathbf{v}_i - \mathbf{v}_e| \ll |\mathbf{v}_i - \mathbf{v}|$), so the field is effectively frozen also into the ions, whereas in the Hall regime the ions and neutrals essentially move together and the electrons drift relative to them ($|\mathbf{v}_i - \mathbf{v}_e| \gg |\mathbf{v}_i - \mathbf{v}|$). More generally, one can define an effective velocity \mathbf{v}_B for the poloidal flux surfaces that applies also in the Ohm regime, when these surfaces are no longer frozen into any particle species (although, as noted in Sect. 2.1, they continue to maintain their identity). Focusing on the midplane, where $B = B_z$, this is done through the relation $c\mathbf{E} = -\mathbf{v}_B \times \mathbf{B}$ (cf. Umebayashi & Nakano 1986). As we just observed, in the absence of Ohm diffusivity (and still considering only ion and electron charges) this relation is satisfied if one substitutes \mathbf{v}_e for the velocity, which verifies that $\mathbf{v}_B = \mathbf{v}_e$ in this case. However, in the Ohm regime the azimuthal field-line velocity

$$v_{B\phi,0} = -cE_{r,0}/B_0 \quad (21)$$

can differ from that of the most mobile charged particle component, and similarly for the radial flux-surface velocity

$$v_{Br,0} = cE_{\phi,0}/B_0 , \quad (22)$$

where the subscript ‘0’ denotes the midplane.

A departure from ideal MHD may lead to energy dissipation at a rate (per unit volume) $\mathbf{J} \cdot \mathbf{E}'$. As can be inferred from Eqs. (7) and (15), both the Ohm and ambipolar terms in Ohm’s law contribute to Joule heating, but not the Hall term. It may perhaps seem puzzling that energy is dissipated in the ambipolar regime even though the field lines remain frozen to the charged particles, but one can directly associate the heating in this case with the ion-neutral collisional drag: $\mathbf{J} \cdot \mathbf{E}' \approx n_i \mathbf{v}_{d,i} \cdot \mathbf{F}_{in}$ (assuming $Z_i \gg 1$; see Eqs. (8) and (11)). Joule dissipation would be the main internal heating mechanism in disk regions where angular momentum transport is dominated by a large-scale, ordered field. Ambipolar heating, in particular, could also play an important role in the thermal structure of disk-driven winds (see Sect. 4.3).

Just as we arrived at a combination of physical variables that measures the degree of coupling between a charged particle and the magnetic field (namely,

the Hall parameter; Eq. (9)), we will find it useful to identify an analogous measure for the neutrals. It turns out that an appropriate parameter combination of this type for Keplerian disks, which plays a similar role in MRI-based systems (where the neutrals couple to a small-scale, disordered field) and in wind-driving disks (where the coupling is to a large-scale, ordered field), is the *Elsasser number*

$$A \equiv \frac{v_A^2}{\Omega_K \eta_\perp}, \quad (23)$$

where

$$\eta_\perp = \frac{c^2}{4\pi\sigma_\perp} \quad (24)$$

is the “perpendicular” magnetic diffusivity and Ω_K is the Keplerian angular velocity. This parameter is $\gg 1$ and $\ll 1$ for strong and weak neutral-field coupling, respectively.⁶ The Elsasser number is used in planetary dynamo theory to measure the ratio of the Lorentz to Coriolis forces. Since both the MRI mechanism and the field-mediated vertical angular momentum transport involve magnetic coupling to Keplerian rotation, it is not surprising that this parameter also arises in the disk context. In the three main conductivity regimes it reduces to

$$A \Rightarrow \begin{cases} \frac{\gamma_i \rho_i}{\Omega_K} \equiv \mathcal{Y} & \text{ambipolar} \\ \beta_i \mathcal{Y} & \text{Hall} \\ \beta_e \beta_i \mathcal{Y} & \text{Ohm,} \end{cases} \quad (25)$$

where we again assumed, for simplicity, that the only charged particles are ions and electrons. The ambipolar limit has a clear physical meaning: it represents the ratio \mathcal{Y} of the Keplerian rotation time to the neutral-ion momentum-exchange time. This parameter has emerged as the natural measure of the field-matter coupling in the wind-driving disk models of Wardle & Königl (1993; see Sect. 4.4) as well as in studies of the linear (e.g., Blaes & Balbus 1994) and nonlinear (e.g., Mac Low et al. 1995; Brandenburg et al. 1995; Hawley & Stone 1998) evolution of the MRI in such disks. Indeed, since the ions are well coupled to the field in this limit ($|\beta_i| \gg 1$), the neutrals will be well coupled to the field if their momentum exchange with the charged particles (which is dominated by their interaction with the comparatively massive ions) occurs on a time scale that is short in comparison with the dynamical time Ω_K^{-1} (corresponding to $\mathcal{Y} > 1$). In the Hall regime A is equal to this ratio of time scales multiplied by $|\beta_i|$. This product has figured prominently in the

⁶ The parameter A is distinct from the Lundquist number $S \equiv v_A L / \eta_O$ and from the magnetic Reynolds number $\text{Re}_M \equiv VL / \eta_O$ (where V and L are characteristic speed and length-scale, respectively), which have been used in similar contexts in the literature. It was first introduced into the protostellar disk literature in this form (but using a different symbol) by Wardle (1999).

classification of wind-driving disk solutions (Königl et al. 2010) as well as in linear studies of disk MRI in this regime (e.g., Wardle 1999; Balbus & Terquem 2001). In this case, too, it has a clear physical meaning. In contradistinction to the ambipolar regime, the *ions are not well coupled* to the field in the Hall limit ($|\beta_i| \ll 1$). In order for the neutrals to be well coupled to the field it is, therefore, not sufficient for them to be well coupled to the ions ($\mathcal{Y} > 1$); rather, the product $|\beta_i|\mathcal{Y}$ must be > 1 in this case. In the Ohm regime, even *the electrons are not well coupled* to the field ($|\beta_e| \ll 1$), so now the product $\beta_e\beta_i\mathcal{Y}$ has to exceed 1 to ensure an adequate coupling of the neutrals to the field. The condition $\Lambda \gtrsim 1$ in fact characterizes both the linear (e.g., Jin 1996) and the nonlinear (e.g., Sano et al. 2002) behavior of the MRI in this regime, and the Elsasser number is again a natural parameter for classifying viable wind-driving disk solutions in this case (with each sub-regime corresponding to a distinct lower bound on Λ ; see Königl et al. 2010).

2.5 Similarity Solutions

Even the most simplified models of magnetically threaded protostellar disks lead to systems of nonlinear partial differential equations (PDEs). In some cases, such as the disk–star interaction considered in Sect. 5, it has proven necessary to carry out full-fledged numerical simulations to get definitive answers about the expected behavior. However, for other aspects of the problem, such as the disk formation (Sect. 3) and the wind-driving disk structure (Sect. 4), it has been possible to make analytic (or, rather, semianalytic) progress by looking for *similarity solutions*, an approach that converts the PDEs into ordinary differential equations (ODEs; e.g., Landau & Lifshitz 1987). This type of solution does not incorporate either inner or outer radial boundaries, so it can be justified only at radii that are sufficiently far removed from the disk’s actual edges. However, the basic properties revealed by these solutions have invariably been confirmed by simulations, and the analytic approach has the advantage of making the qualitative behavior more transparent and of making it possible to better investigate the parameter dependence of the solutions and to incorporate more physics and dynamic range than is yet possible numerically. The semianalytic and numerical approaches have thus played complementary roles in shedding light on these questions.

In the case of the disk-formation problem, the separate dependences on the spatial scale r and the time t are subsumed into a single dependence on the dimensionless combination r/Ct , taking advantage of the fact that the isothermal sound speed C is nearly uniform (on account of the efficient cooling by dust grains) in cloud cores and in the outer regions of circumstellar disks. The self-similarity of the derived solutions is expressed by the fact that they depend solely on the ratio r/t and not on the separate values of r and t . In the case of the stationary, axisymmetric wind-driving disk models, the separate dependences on the spatial coordinates z and r are subsumed into a single dependence on the dimensionless combination z/r (or, equivalently,

on $z(r, r_0)/r_0$, where $z(r, r_0)$ describes the shape of a magnetic field line that intersects the midplane at r_0). In these *radially self-similar* models all physical variables scale as power laws of the *spherical* radius $R = (z^2 + r^2)^{1/2}$ and the differential equations depend only on the polar angle $\theta = \text{arc cot}(z/r)$. Further details are given in Secs. 3 and 4, respectively.

3 Disk Formation and Early Evolution

Rotationally supported circumstellar disks evidently originate in the collapse of self-gravitating, rotating, molecular cloud cores. Molecular line observations (e.g., Goodman et al. 1993; Kane & Clemens 1997) have established that a majority of dense ($\gtrsim 10^4 \text{ cm}^{-3}$) cloud cores show evidence of rotation, with angular velocities $\sim 3 \times 10^{-15} - 10^{-13} \text{ s}^{-1}$ that tend to be uniform on scales of $\sim 0.1 \text{ pc}$, and with specific angular momenta in the range $\sim 4 \times 10^{20} - 3 \times 10^{22} \text{ cm}^2 \text{ s}^{-1}$. The cores can transfer angular momentum to the ambient gas by magnetic braking (Sect. 2.2), and this mechanism also acts to align their angular momentum vectors with the local large-scale magnetic field (e.g., Machida et al. 2006). This alignment occurs on a dynamical time scale and hence can be achieved even in cores whose lifetimes are not much longer than that (as in certain models of the turbulent ISM; e.g., Elmegreen 2000). The dynamical collapse might occur as a result of mass rearrangement in the core on the ambipolar diffusion time (e.g., Mouschovias et al. 2006; see Sect. 2.4) or sooner if the core is close to the critical mass for collapse (the effective Jeans mass) from the start (e.g., Elmegreen 2007). In this section we consider the core collapse problem in the context of angular momentum transport by a large-scale, ordered magnetic field; an alternative scenario involving gravitational torques is discussed in Chap. IV.

Once dynamical collapse is initiated and a core goes into a near-free-fall state, the specific angular momentum is expected to be approximately conserved, resulting in a progressive increase in the centrifugal force that eventually halts the collapse and gives rise to a rotationally supported disk on scales $\sim 10^2 \text{ AU}$. These expectations are consistent with the results of molecular-line interferometric observations of contracting cloud cores (e.g., Ohashi et al. 1997; Belloche et al. 2002). In this picture, the disk rotation axis should be aligned with the direction of the large-scale magnetic field that threads the cloud. Observations have not yet yielded a clear-cut answer to whether this is indeed the case in reality (e.g., Ménard & Duchêne 2004; Vink et al. 2005), and it is conceivable that the field in some cases is too weak to align the core's rotation axis or even control its contraction, or that additional processes (such as fragmentation, disk warping, etc.) play a role. In what follows we nevertheless continue to pursue the implications of the basic magnetically supported cloud picture.

3.1 Modeling Framework

Since the gravitational collapse time is much shorter than the local ambipolar diffusion time in the core, the magnetic field lines at first move in with the infalling matter. However, once the central mass begins to grow, ambipolar diffusion becomes important within the gravitational “sphere of influence” of the central mass (Ciolek & Königl 1998; Contopoulos et al. 1998). When the incoming matter enters this region, it decouples from the field and continues moving inward. The decoupling front, in turn, moves outward and steepens into an *ambipolar diffusion shock*. The existence of this C-type MHD shock was first predicted by Li & McKee (1996). The transition from a nearly freely falling, collapsing core to a quasi-stationary, rotationally supported disk involves a strong deceleration in a *centrifugal shock*. This shock typically occurs at a smaller radius than the ambipolar-diffusion shock and is hydrodynamic, rather than hydromagnetic, in nature.

Based on the arguments presented in Sect. 2.1 it should be a good approximation to assume that the gas rapidly establishes force equilibrium along the field and therefore to consider only motions in the radial direction.⁷ One can obtain semianalytic solutions for this effectively 1D time-dependent problem by postulating $r - t$ self-similarity, with a similarity variable

$$x \equiv \frac{r}{Ct} \quad (26)$$

(see Sect. 2.5). This modeling approach is motivated by the fact that core collapse is a *multiscale* problem, which is expected to assume a self-similar form away from the outer and inner boundaries and not too close to the onset time (e.g., Penston 1969; Larson 1969; Hunter 1977; Shu 1977). This has been verified by numerical and semianalytic treatments of restricted core-collapse problems – with/without rotation and with/without magnetic fields. Although the constancy of the isothermal sound speed C that underlies the ansatz (26) is not strictly maintained throughout the solution domain (in particular, C scales roughly as $r^{-1/2}$ in large portions of the disk that forms around the central star), this is of little consequence to the results since thermal stresses do not play a major role in the dynamics of the collapsing core. For a typical sound speed $C = 0.19 \text{ km s}^{-1}$, $x = 1 \Leftrightarrow \{400, 4000\} \text{ AU}$ at $t = \{10^4, 10^5\} \text{ yr}$.

Krasnopolsky & Königl (2002, hereafter KK02) constructed self-similar solutions of rotating magnetic molecular cloud cores that are subject to ambipolar diffusion. These solutions reveal many of the basic features of star and disk formation in the core-collapse scenario and are discussed in the remainder of this section. To incorporate ambipolar diffusion into the self-similarity

⁷ In reality, mass can also be added to the system from the polar directions. Numerical simulations of axisymmetric collapse in which new mass is added *only* through vertical infall have tended to produce disk-to-star mass ratios ~ 1 , much higher than typically observed. A better agreement with observations may, however, be obtained when nonaxisymmetric density perturbations and resultant gravitational torques are included in the calculations (e.g., Vorobyov & Basu 2007).

formulation it is necessary to assume that the ion density scales as the square root of the neutral density: $\rho_i = \mathcal{K}\rho^{1/2}$. As discussed in KK02, this should be a good approximation for the core-collapse problem: it applies on both ends of a density range spanning ~ 8 orders of magnitude, which corresponds roughly to radial scales $\sim 10 - 10^4$ AU, with \mathcal{K} varying by only ~ 1 order of magnitude across this interval.

To allow mass to accumulate at the center in a 1D rotational collapse, an angular momentum transport mechanism must be present. KK02 assumed that *vertical* transport through magnetic braking continues to operate also during the collapse phase of the core evolution. To incorporate this mechanism into the self-similar model it is necessary to assume that v_{Aext} , the Alfvén speed in the external medium, is a constant.⁸ KK02 verified that, in their derived solutions, magnetic braking indeed dominates the most likely alternative angular-momentum transport mechanisms — MRI-induced turbulence and gravitational torques. However, they also found that angular momentum transport by a CDW arises naturally (and may dominate) in the Keplerian disk that forms in their fiducial solution (see Sect. 3.4).

3.2 Basic Equations

The mass and momentum conservation relations in their *differential* form are given by:

Mass

$$\frac{\partial \rho}{\partial t} + \frac{1}{r} \frac{\partial}{\partial r} (r \rho v_r) = - \frac{\partial}{\partial z} (\rho v_z), \quad (27)$$

Radial Momentum

$$\begin{aligned} \rho \frac{\partial v_r}{\partial t} + \rho v_r \frac{\partial v_r}{\partial r} = & \rho g_r - C^2 \frac{\partial \rho}{\partial r} + \rho \frac{v_\phi^2}{r} + \frac{B_z}{4\pi} \frac{\partial B_r}{\partial z} \\ & - \frac{\partial}{\partial r} \left(\frac{B_z^2}{8\pi} \right) - \frac{1}{8\pi r^2} \frac{\partial}{\partial r} (r B_\phi)^2 - \rho v_z \frac{\partial v_r}{\partial z}, \end{aligned} \quad (28)$$

Angular Momentum

$$\frac{\rho}{r} \frac{\partial}{\partial t} (r v_\phi) + \frac{\rho v_r}{r} \frac{\partial}{\partial r} (r v_\phi) = \frac{B_z}{4\pi} \frac{\partial B_\phi}{\partial z} + \frac{B_r}{4\pi r} \frac{\partial}{\partial r} (r B_\phi) - \rho v_z \frac{\partial}{\partial z} (r v_\phi), \quad (29)$$

Vertical Hydrostatic Equilibrium

$$C^2 \frac{\partial \rho}{\partial z} = \rho g_z - \frac{\partial}{\partial z} \left(\frac{B_\phi^2}{8\pi} + \frac{B_r^2}{8\pi} \right) + \frac{B_r}{4\pi} \frac{\partial B_z}{\partial r}, \quad (30)$$

⁸ A nearly constant value $v_{\text{Aext}} \approx 1 \text{ km s}^{-1}$ is, in fact, indicated in molecular clouds in the density range $\sim 10^3 - 10^7 \text{ cm}^{-3}$ (e.g., Crutcher 1999).

where g_r and g_z are, respectively, the radial and vertical components of the gravitational acceleration. We have not yet dropped the terms that involve the vertical velocity component (except in the vertical momentum equation, which we assume takes on its hydrostatic form).

We now integrate these equations over the core/disk thickness $2H$. We use the *thin-disk approximation* ($H(r) \ll r$) and assume that the density, radial velocity, azimuthal velocity, and radial gravity are constant with height, and that so is also B_z (except when it is explicitly differentiated with respect to z , in which case we substitute $\partial B_z/\partial z = -r^{-1}(\partial/\partial r)(rB_r)$ from $\nabla \cdot \mathbf{B} = 0$). We also assume $B_r(r, z) = B_{r,s}(r)[z/H(r)]$ (and similarly for B_ϕ), and, after deriving expressions that are valid to order $(H/r)^2$, further simplify by dropping all terms $\mathcal{O}(H/r)$ except in the combination $[B_{r,s} - H(\partial B_z/\partial r)]$ (see KK02 for details). We thus obtain the *vertically integrated* conservation equations:

Mass

$$\frac{\partial \Sigma}{\partial t} + \frac{1}{r} \frac{\partial}{\partial r} (r \Sigma v_r) = -\frac{1}{2\pi r} \frac{\partial \dot{M}_w}{\partial r}, \quad (31)$$

Radial Momentum

$$\frac{\partial v_r}{\partial t} + v_r \frac{\partial v_r}{\partial r} = g_r - \frac{C^2}{\Sigma} \frac{\partial \Sigma}{\partial r} + \frac{B_z}{2\pi \Sigma} \left(B_{r,s} - H \frac{\partial B_z}{\partial r} \right) + \frac{J^2}{r^3}, \quad (32)$$

Angular Momentum

$$\frac{\partial J}{\partial t} + v_r \frac{\partial J}{\partial r} = \frac{r B_z B_{\phi s}}{2\pi \Sigma}, \quad (33)$$

Vertical Hydrostatic Equilibrium

$$\frac{\Sigma C^2}{2H} = \frac{\pi}{2} G \Sigma^2 + \frac{GM_* \rho H^2}{2r^3} + \frac{1}{8\pi} \left(B_{\phi,s}^2 + B_{r,s}^2 - B_{r,s} H \frac{\partial B_z}{\partial r} \right), \quad (34)$$

where $\Sigma = 2\rho H$ is the surface mass density, $J = rv_\phi$ is the specific angular momentum of the matter, G is the gravitational constant, and M_* is the mass of the central protostar. In the integrated equations we have implemented the 1D flow approximation by setting $v_z = 0$, but we retained the term on the right-hand side of Eq. (31) to allow for mass loss through a disk wind (at a rate \dot{M}_w). Such a wind could carry angular momentum, but we did not include vertical particle angular momentum transport in Eq. (33) since most of a disk wind's angular momentum initially resides in the magnetic field (see Sect. 4.3). In any case, we proceed to solve the equations by assuming at first that no wind is present and that the only mechanism of angular momentum transport is magnetic braking.

The dominant charge carriers in the pre-collapse core are ions and electrons. Adopting this composition, we approximate the *ion equation of motion* in the ambipolar-diffusion limit by

$$\varrho\nu_{\text{ni}}\mathbf{v}_d = \frac{1}{4\pi}(\nabla \times \mathbf{B}) \times \mathbf{B}, \quad (35)$$

where ν_{ni} is the neutral-ion collision frequency (see Eqs. (8) and (10)). This relation yields the components of the drift velocity:

$$v_{d,\phi} = \frac{B_z B_{\phi,s}}{2\pi\nu_{\text{ni}}\Sigma}, \quad (36)$$

$$v_{d,r} = \frac{B_z}{2\pi\nu_{\text{ni}}\Sigma} \left(B_{r,s} - H \frac{\partial B_z}{\partial r} \right). \quad (37)$$

Magnetic braking is incorporated via Eq. (4), in which we identify $v_{b\phi}$ with $v_{i,\phi}$ (see Sect. 2.4). Expressing $v_{i,\phi}$ in terms of v_ϕ and $v_{d,\phi}$ (Eq. (36)) and imposing a cap ($\delta \lesssim 1$) on $|B_{\phi,s}/B_z|$ (to account for the possible development of a kink instability above the disk surface), one gets

$$B_{\phi,s} = -\min \left[\frac{\Psi}{\pi r^2} \frac{v_\phi}{v_{\text{Aext}}} \left(1 + \frac{\Psi B_z}{2\pi^2 r^2 \nu_{\text{ni}} \Sigma v_{\text{Aext}}} \right)^{-1}, \delta B_z \right]. \quad (38)$$

The flux conservation relation $\partial\Psi/\partial t = -2\pi r v_{Br} B_z$ (obtained from Eqs. (20) and (22)), which describes the advection of poloidal flux by the infalling matter, can be written in this limit as

$$\frac{\partial\Psi}{\partial t} = -2\pi r v_{i,r} B_z = -2\pi r (v_r + v_{d,r}) B_z, \quad (39)$$

with $v_{d,r}$ given by Eq. (37). The surface value of B_r that appears in the latter equation can be determined in the limit of a potential field ($\nabla \times \mathbf{B} = 0$) outside an infinitely thin disk from an r integral of the midplane value of B_z :

$$B_{r,s} = \int_0^\infty dk J_1(kr) \int_0^\infty dr' r' [B_z(r') - B_{\text{ref}}] J_0(kr') \quad (40)$$

(e.g., Ciolek & Mouschovias 1993), where J_0 and J_1 are Bessel functions of order 0 and 1, respectively, and B_{ref} is the uniform ambient field at “infinity” (which is henceforth neglected). Although the current-free limit of the force-free medium outside the core/disk is not exact, as the presence of a B_ϕ component, which typically involves a distributed poloidal electric current, is required for angular momentum transport above and below the core/disk surfaces, the magnitude of $|B_{\phi,s}/B_z|$ (as deduced from Eq. (38)) is typically small at the start of the collapse (e.g., Basu & Mouschovias 1994). Furthermore, even after this ratio increases to ~ 1 as matter and field become concentrated near the center, the magnitude of the enclosed (poloidal) current ($I = (c/2)r|B_\phi|$) increases relatively slowly with decreasing r (scaling as $r^{-1/4}$ in the circumstellar disk; see Eq. (55) below), so overall we expect the expression (40) to be a fair approximation. A similar integral (with $\Sigma(r)$ replacing B_z) can be written for g_r (Toomre 1963). These integrals can be approximated by their *monopole* terms

$$B_{r,s} = \frac{\Psi(r, t)}{2\pi r^2}, \quad (41)$$

$$g_r = -\frac{GM(r, t)}{r^2} \quad (42)$$

(cf. Li & Shu 1997), where $M(r, t)$ is the mass enclosed within a radius r at time t . When $B_z(r)$ (or $\Sigma(r)$) scales as r^{-q} , one still obtains the monopole expression for $B_{r,s}$ (or g_r), but with a q -dependent coefficient $\mathcal{O}(1)$ (Ciolek & Königl 1998).

3.3 Self-Similarity Formulation

The various physical quantities of the problem can be expressed as dimensionless functions of the similarity variable x (Eq. (26)) in the following fashion:

$$H(r, t) = Ct h(x), \quad \Sigma(r, t) = (C/2\pi Gt) \sigma(x), \quad (43)$$

$$v_r(r, t) = C u(x), \quad v_\phi(r, t) = C w(x), \quad (44)$$

$$g_r(r, t) = (C/t) g(x), \quad J(r, t) = C^2 t j(x), \quad (45)$$

$$M(r, t) = (C^3 t/G) m(x), \quad \dot{M}_a(r, t) = (C^3/G) \dot{m}(x), \quad (46)$$

$$\mathbf{B}(r, t) = (C/G^{1/2}t) \mathbf{b}(x), \quad \Psi(r, t) = (2\pi C^3 t/G^{1/2}) \psi(x) \quad (47)$$

where \dot{M}_a is the mass accretion rate.

The vertical force-balance relation (34) yields a quadratic equation for the normalized disk half-thickness h ,

$$\left(\frac{\sigma m_*}{x^3} - b_{r,s} \frac{db_z}{dx} \right) h^2 + (b_{r,s}^2 + b_{\phi,s}^2 + \sigma^2) h - 2\sigma = 0, \quad (48)$$

whose solution is

$$h = \frac{\hat{\sigma} x^3}{2\hat{m}_*} \left[-1 + \left(1 + \frac{8\hat{m}_*}{x^3 \hat{\sigma}^2} \right)^{1/2} \right], \quad (49)$$

where $\hat{m}_* \equiv m_* - x^3 b_{r,s} (db_z/dx)/\sigma$ and $\hat{\sigma} \equiv \sigma + (b_{r,s}^2 + b_{\phi,s}^2)/\sigma$.

The initial ($t = 0$) conditions, which in the self-similar model also represent the *outer asymptotic* ($r \rightarrow \infty$) values, correspond to a collapsing core just before it forms a central point mass. Based on previous analytic and numerical work, KK02 adopted

$$\sigma \rightarrow \frac{A}{x}, \quad b_z \rightarrow \frac{\sigma}{\mu_\infty}, \quad u \rightarrow u_\infty, \quad w \rightarrow w_\infty \quad \text{as } x \rightarrow \infty, \quad (50)$$

with $A = 3$, $\mu_\infty = 2.9$, $u_\infty = -1$. From the constituent equations one can also derive the *inner asymptotic* behavior (corresponding to $r \rightarrow 0$ at a fixed t) in the Keplerian disk:

$$\dot{m} = m = m_*, \quad (51)$$

$$j = m_*^{1/2} x^{1/2}, \quad (52)$$

$$-u = (m_*/\sigma_1) x^{1/2}, \quad (53)$$

$$\begin{aligned} \sigma &= \frac{(2\eta/3\delta)(2m_*)^{1/2}}{[1 + (2\tau/3\delta)^{-2}]^{1/2}} x^{-3/2} \\ &\equiv \sigma_1 x^{-3/2}, \end{aligned} \quad (54)$$

$$b_z = -b_{\phi,s}/\delta = [m_*^{3/4}/(2\delta)^{1/2}] x^{-5/4}, \quad (55)$$

$$b_{r,s} = \psi/x^2 = (4/3)b_z, \quad (56)$$

$$h = \{2/[1 + (2\tau/3\delta)^2]m_*\}^{1/2} x^{3/2}, \quad (57)$$

where $\tau \equiv (4\pi G\rho)^{1/2}/\nu_{\text{ni}}$.

The equations are solved as a boundary value problem using the above asymptotic relations. A solution is determined by the values of the four model parameters: τ , $\delta = |B_{\phi,s}/B_z|$, $w_\infty = v_\phi(t=0)/C$, and $\alpha \equiv C/v_{\text{Aext}}$. The scaling parameter m_* for the central mass and the mass accretion rate is obtained as an eigenvalue of the problem.

3.4 Self-Similar Collapse Solutions

Figure 2 shows a fiducial solution corresponding to the parameter combination $\tau = 1$, $\delta = 1$, $w(0) = 0.73$, and $\alpha = 0.8$ (which yield $m_* = 4.7$). In this case the initial rotation is not very fast and the braking is moderate, leading to the formation of a disk (with outer boundary at the centrifugal shock radius $x_c = 1.3 \times 10^{-2}$) within the ambipolar-diffusion (AD) region (delimited by the AD shock radius $x_a = 0.41 \approx 30x_c$). One can distinguish the following main flow regimes:

- Outer region ($x > x_a$): ideal-MHD infall.
- AD shock: resolved as a continuous transition (but may in some cases contain a viscous subshock); KK02 estimated $x_a \approx \sqrt{2}\tau/\mu_\infty$.
- Ambipolar diffusion-dominated infall ($x_c < x < x_a$): near free fall controlled by the central star's gravity.
- Centrifugal shock: its location depends sensitively on the diffusivity parameter τ , which affects the amount of magnetic braking for $x < x_a$; KK02 estimated $x_c \approx (m_* w_\infty^2/A^2) \exp\{-(2^{3/2}m_*/\mu_\infty)^{1/2}\tau^{-3/2}\}$.
- Keplerian disk ($x < x_c$): asymptotic behavior (Eqs. (51)–(57)) is approached after a transition zone representing a massive ring (of width $\sim 0.1x_c$ and mass $\sim 8\%$ of the disk mass within x_c , which itself is $\lesssim 5\%$ of m_*).

The inner asymptotic solution implies that, at any given time, the disk satisfies $\dot{M}_a(r) = \text{const}$, $\Sigma(r) \propto r^{-3/2}$, $B \propto r^{-5/4}$, and $B_{r,s}/B_z = 4/3$.⁹ If

⁹ The surface density scaling is the same as that inferred for the “minimum mass” solar nebula (e.g., Weidenschilling 1977). Note, however, that this scaling is also

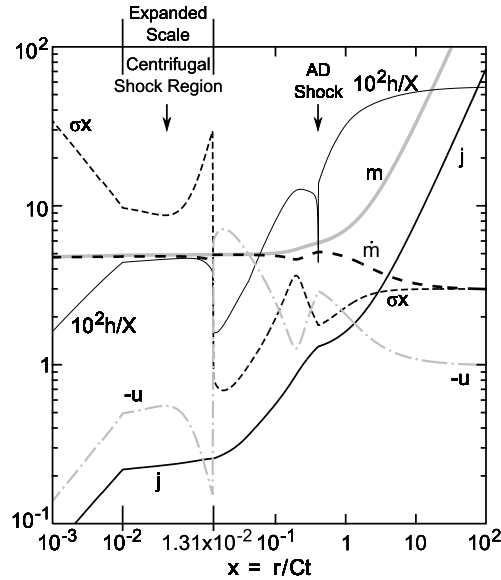


Fig. 2. Behavior of key normalized variables in the fiducial self-similar disk formation solution as a function of the similarity variable x (see Eqs. (43)–(46)).

the derived power-law dependence of B_z on r is used in Eq. (40) one obtains $B_{r,s}/B_z = 1.428$, slightly less than the result found with the monopole approximation (41), but still representing a strong bending of the field lines (by $\sim 55^\circ$ from the normal) that is significantly larger than the minimum of 30° required for launching a centrifugally driven wind from a “cold” Keplerian disk (Eq. (6)). This implies that protostellar disks formed in this fashion are likely to drive disk outflows over much of their radial extents, at least during early times when they still accumulate mass from the collapsing core. Interestingly, the *steady-state, radially self-similar* CDW solution of Blandford & Payne (1982) also yields a radial magnetic field scaling $\propto r^{-5/4}$. As discussed by KK02, this suggests that angular momentum transport by a CDW can be formally incorporated into the disk-formation solution, modifying some of the details (such as the mass accretion rate onto the star, which could be reduced by up to a factor of ~ 3) although not its basic properties. When interpreted as a wind-driving disk model, the asymptotic solution corresponds to a weakly coupled disk configuration (using the nomenclature introduced in Sect. 4.4).

Despite being based on a number of simplifying assumptions, the fiducial solution demonstrates that vertical angular momentum transport along inter-

predicted for a self-similar Keplerian disk with an “ α viscosity” (Tsuribe 1999) as well as in certain models in which gravitational torques dominate the angular momentum transport (e.g., Lin & Pringle 1987; Voroboyov & Basu 2007).

stellar magnetic field lines can be sufficiently efficient to allow most of the mass of a collapsing molecular cloud core to end up (with effectively no angular momentum) at the center, with the central mass dominating the dynamics well beyond the outer edge of the disk even as the inflow is still in progress. The vertical transport is thus seen to resolve the so-called angular momentum problem in star formation (although the exact value of the protostar’s angular momentum is determined by processes near the stellar surface that are not included in this model; see Sect. 5). To the extent that self-similarity is a good approximation to the situation in such cores, it is conceivable that T Tauri (Class II) protostellar systems, whose disk masses are typically inferred to be $\lesssim 10\%$ of the central mass, have had a similarly low disk-to-star mass ratio also during their earlier (Class 0 and Class I) evolutionary phases. This possibility remains to be tested by observations.

The fiducial solution also reveals that the AD shock, even though it is located well outside the region where the centrifugal force becomes important, helps to enhance the efficiency of angular momentum transport through the magnetic field amplification that it induces. The revitalization of ambipolar diffusion behind the AD shock in turn goes a long way toward resolving the magnetic flux problem in star formation (the several-orders-of-magnitude discrepancy between the empirical upper limit on the magnetic flux of a protostar and the flux associated with the corresponding mass in the pre-collapse core), although it is conceivable that Ohm diffusivity in the innermost regions of the disk also plays an important role in this process (e.g., Shu et al. 2006; Tassis & Mouschovias 2007). The details of the flux detachment outside the Ohm regime can be modified if one takes account of the fact that the flux is strictly frozen into the electrons but not necessarily into the ions (i.e., if one includes also the Hall term in Ohm’s Law; see Sect. 2.4). In particular, Tassis & Mouschovias (2005) found that a quasi-periodic series of outward-propagating shocks may develop in this case.

The shocks that form in the collapsing core, and in particular the centrifugal shock (which is the strongest), will process the incoming material and may have implications to the composition of protoplanetary disks (e.g., the annealing of silicate dust; see Harker & Desch 2002 and Chap. VIII [Dust Processing and Mineralogy in Protoplanetary Accretion Disks]). Note in this connection that the shock velocity v_{sh} relative to the intercepted matter has roughly the free-fall magnitude $\propto (M/r)^{1/2}$, which is constant for any given value (including, in particular, x_c) of the similarity variable. The postshock temperature (which scales as $v_{\text{sh}}^{1/2}$) will thus not vary with time if the inflow remains self-similar; the postshock density, on the other hand, will decrease with time as the shock moves to larger radii.

By modifying the model parameters, one can study the range of possible behaviors in real systems. Figure 3 shows two limiting cases, which bracket the fiducial solution (cf. Fig. 2).

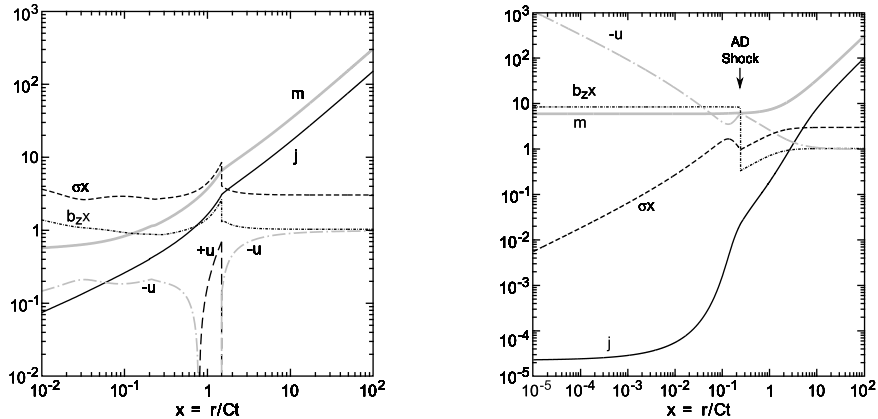


Fig. 3. Behavior of key normalized variables in representative fast-rotation (**left**) and strong-braking (**right**) solutions of the collapse of a rotating, magnetic, molecular cloud core as a function of the similarity variable x (see Eqs. (43)–(47)).

The *fast rotation* case differs from the fiducial solution primarily in having a large initial-rotation parameter ($w(0) = 1.5$). It has the following distinguishing features:

- The centrifugal shock is located within the self-gravity-dominated (and ideal-MHD) region; a back-flowing region is present just behind the shock.
- The central mass is comparatively small ($m_* = 0.5$), giving rise to a non-Keplerian outer disk region.
- The ideal-MHD/ambipolar-diffusion transition occurs behind the centrifugal shock and is gradual rather than sharp.

The *strong braking* case ($\tau = 0.5$, $\delta = 10$, $w(0) = 1$, $\alpha = 10$, yielding $m_* = 5.9$) is characterized by large values of the braking parameters δ and α . It is distinguished by having

- no centrifugal shock (or circumstellar disk); essentially all the angular momentum is removed well before the inflowing gas reaches the center, and the $x \rightarrow 0$ behavior resembles that of the nonrotating collapse solution of Contopoulos et al. (1998).

This case may be relevant to the interpretation of slowly rotating young stars that show no evidence of a circumstellar disk (e.g., Stassun et al. 1999, 2001), which would seem puzzling if all protostars were born with significant rotation that could only be reduced as a result of their interaction with a disk (see Sect. 5). In the strong-braking interpretation, both the slow rotation and the absence of a disk have the same cause. It is also worth noting in this connection that the physical conditions that underlie the fiducial solution presented above — namely, a highly flattened, magnetized core whose braking

is controlled by the inertia of a comparatively low-density ambient gas — may not be generally applicable. In particular, it has been argued (see Mellon & Li 2009 and references therein) that magnetized molecular clouds may retain a significant amount of mass outside the collapsing core that would dominate the braking process and could place the core in the strong-braking regime where disk formation would be suppressed. Although there may be ways to alleviate or even circumvent this problem (e.g., Hennebelle & Ciardi 2009; Duffin & Pudritz 2009), there is obviously a need for additional observational and theoretical work to clarify the physical conditions that characterize core collapse in real clouds.

While the semianalytic self-similarity model described in this section is useful for identifying important features of disk formation from the collapse of rotating cores, the intricacies of this process can only be studied numerically. Newly developed 3D, nonideal-MHD, nested-grid codes (e.g., Machida et al. 2007) are already starting to provide new insights into this problem.

4 Wind-Driving Protostellar Disks

In this section we discuss wind-driving disk models. We begin by highlighting the observational evidence for a close link between outflows and accretion disks in protostellar systems and the interpretation of this connection in terms of a large-scale magnetic field that mediates the accretion and outflow processes. We next outline the theory of centrifugally driven winds, describe the incorporation of CDWs into equilibrium disk models, and conclude by addressing the stability of such disk/wind configurations.

4.1 The Disk–Wind Connection

We give a brief survey of the observational findings on protostellar outflows and their connection to accretion disks. Besides the explicit references cited, the reader may consult some of the many review articles written on this topic over the years (e.g., Cabrit 2007; Calvet et al. 2000; Dutrey et al. 2007; Königl & Pudritz 2000; Millan-Gabet et al. 2007; Najita et al. 2007; Ray et al. 2007; Watson et al. 2007).

Bipolar Outflows and Jets

Bipolar molecular outflows and narrow atomic (but sometimes also molecular) jets are ubiquitous phenomena in protostars, with nearly 1000 collimated outflows of all sorts already known (e.g., Bally et al. 2007). The bipolar lobes are usually understood to represent ambient molecular material that has been swept up by the much faster, highly supersonic jets and winds that emanate from the central star/disk system (e.g., Arce et al. 2007). Jets associated with

low-bolometric-luminosity ($L_{\text{bol}} < 10^3 L_{\odot}$) protostars have velocities in the range $\sim 150 - 400 \text{ km s}^{-1}$, large (> 20) Mach numbers, and inferred mass outflow rates $\sim 10^{-9} - 10^{-7} M_{\odot} \text{ yr}^{-1}$. They are collimated on scales of a few 10s of AU and exhibit opening angles as small as $\sim 3 - 5^{\circ}$ on scales of $10^3 - 10^4$ AU. High-resolution observations of optically visible jets from classical T Tauri stars (CTTSs) reveal an onion-like morphology, with the regions closer to the axis having higher velocities and excitations and appearing to be more collimated. Detailed optical/near-IR spectral diagnostic techniques have been developed and applied to classical (Herbig-Haro) protostellar jets, making it possible to directly estimate the neutral densities in the forbidden-line emission regions. Recent results (Podio et al. 2006) yield an average mass outflow rate of $5 \times 10^{-8} M_{\odot} \text{ yr}^{-1}$, markedly higher than previous estimates. Outflows have also been detected by optical observations of intermediate-mass ($\sim 2 - 10 M_{\odot}$) Herbig Ae/Be stars and other high-luminosity sources. The jet speeds and mass outflow rates in these protostars are larger by a factor $\sim 2 - 3$ and $\sim 10 - 100$, respectively, than in the low- L_{bol} objects.

The Link to Accretion Disks

Strong correlations are found between the presence of *outflow signatures* (P-Cygni line profiles, forbidden line emission, thermal radio radiation, well-developed molecular lobes) and *accretion diagnostics* (UV, IR, and millimeter emission excesses, inverse P-Cygni line profiles) in T Tauri stars (e.g., Hartigan et al. 1995). Such correlations evidently extend smoothly to protostars with masses of $\sim 10 M_{\odot}$. A related finding is that the apparent decline in outflow activity with stellar age follows a similar trend exhibited by disk frequency and inferred mass accretion rate. In addition, correlations of the type $\dot{M} \propto L_{\text{bol}}^q$ (with $q \sim 0.6 - 0.7$) have been found in both low- L_{bol} and high- L_{bol} protostars for mass *accretion* rates and for mass *outflow* rates in ionized jets as well as in bipolar molecular lobes. Furthermore, CTTS-like accretion and outflow phenomena have now been detected also in very-low-mass stars and brown dwarfs (e.g., Mohanty et al. 2005).

These findings strongly suggest that outflows are powered by accretion and that the same basic physical mechanism operates in both low- (down to nearly the planetary mass limit) and intermediate-mass protostars, and possibly also in some higher-mass objects (e.g., Shepherd 2005). The accretion proceeds through circumstellar disks, which can be directly probed by means of high spectral- and spatial-resolution (in particular, interferometric) observations at submillimeter, millimeter, mid-IR, near-IR, and optical wavelengths. The disks appear to be rotationally supported (for $r \lesssim 100 \text{ AU}$), and when the rotation law can be determined, it is usually consistent with being Keplerian ($v_{\phi} \propto r^{-1/2}$). Recent data indicate that $M_{\text{disk}} \lesssim M_{*}$ at least up to $M_{*} \sim 20 M_{\odot}$.

Strong evidence for a disk origin for the observed outflows is available for *FU Orionis outbursts* in rapidly accreting young protostars (e.g., Hart-

mann & Kenyon 1996). It is inferred that the emission during an outburst (of typical duration $\sim 10^2$ yr) originates in a rotating disk and that the outflow represents a wind that accelerates from the disk surface (with $\dot{M}_w/\dot{M}_a \sim 0.1$; $\dot{M}_a \sim 10^{-4} M_\odot \text{ yr}^{-1}$). It has been suggested (Hartmann 1997) that most of the mass accumulation and ejection in low-mass protostars occurs during recurrent outbursts of this type. Interestingly, estimates in CTTSs (e.g., Kurosawa et al. 2006; Ray et al. 2007) indicate that \dot{M}_w/\dot{M}_a has a similar value (i.e., ~ 0.1) also during the quiescent phases of these protostars.

4.2 Magnetic Driving of Protostellar Outflows

The most widely accepted explanation of protostellar outflows is that they tap the rotational kinetic energy of the disk (and/or central object) and are accelerated centrifugally from the disk (or stellar) surface by the stress of a large-scale, ordered magnetic field that threads the source. In this subsection we review the arguments that have led to this picture and list a few alternatives for the origin of the field.

Outflow Driving Forces

The momentum discharges inferred from observations of protostellar jets are compatible with the values deduced for the bipolar molecular outflows but are typically a factor $\sim 10^2 - 10^3$ higher than the radiation-pressure thrust L_{bol}/c produced by the stellar luminosity, ruling out *radiative acceleration* as a dominant driving mechanism in low/intermediate-mass protostars (e.g., Richer et al. 2000). Radiative effects could however be important in driving photoevaporative disk outflows, particularly in high- L_{bol} systems (e.g., Hollenbach et al. 1994; see Chap. VII [The Dispersal of Disks around Young Stars]). Disk heating by a luminous protostar (such as a Herbig Be star) could potentially also induce a line-driven wind from the inner disk (Drew et al. 1998). Another effect is radiation pressure on the dusty outer regions of a disk wind, which could act to decollimate the streamlines even in comparatively low- L_{bol} systems (see Sect. 4.3 and cf. Königl & Kartje 1994).

Thermal pressure acceleration is commonly discounted as a dominant mechanism since the requisite high (effectively virial) temperatures are not generally observed at the base of the flow. It has, however, been suggested that, under suitable conditions, the thermal energy released in shocks at the boundary layer between the disk and the star could be efficiently converted into outflow kinetic energy (Torbett 1984; Soker & Regev 2003). Even if this is not a dominant mechanism, thermal pressure effects are nevertheless important in the mass loading of hydromagnetic winds (see Sect. 4.3) and could potentially also play a significant role in the initial acceleration of disk outflows of this type (e.g., Pesenti et al. 2004).

A general result for protostellar jets can be obtained by combining

1. $\dot{M}_{\text{jet}} v_{\text{jet}} \sim 10^2 - 10^3 L_{\text{bol}}/c$
2. $L_{\text{jet}} \sim \dot{M}_{\text{jet}} v_{\text{jet}}^2$
3. $v_{\text{jet}} \sim 10^{-3} c$
4. $L_{\text{bol}} \sim L_{\text{acc}} (\sim GM_* \dot{M}_a/R_*)$

(where R_* is the stellar radius), which implies that, on average, the jet kinetic luminosity is related to the released accretion luminosity by $L_{\text{jet}} \sim 0.1 - 1 L_{\text{acc}}$.¹⁰ Such a high ejection efficiency is most naturally understood if the jets are driven *hydromagnetically* (see Eqs. (68) and (70) below). This mechanism also provides a natural explanation of the strong collimation exhibited by protostellar jets (see Sect. 4.3).

Origin of Large-Scale Disk Magnetic Field

Perhaps the most likely origin of a large-scale, open magnetic field that can launch a CDW from a protostellar disk is the interstellar field that supports the natal molecular cloud core. We have already considered the observational evidence for such a core-threading field (Sect. 1), its dynamical effect on the core (Sect. 2.1), and how it is advected inward by the inflowing matter during gravitational collapse (Sect. 3). However, to complete the argument it is still necessary to demonstrate that, once a rotationally supported disk is established, magnetic flux that is brought in to its outer edge remains sufficiently well coupled to the inflowing matter to be distributed along the disk plane. A potential problem arises, however, in turbulent disks in which only radial angular momentum transport is present. In particular, in a disk of characteristic radius R and half-thickness $H \ll R$ in which angular momentum transport is due to an effective turbulent viscosity ν_{turb} , inward dragging of magnetic field lines is possible only if the effective turbulent magnetic diffusivity η_{turb} satisfies $\eta \lesssim (H/R)\nu$,¹¹ which may not occur naturally in such a system (Lubow et al. 1994a).¹² The introduction of vertical angular momentum transport along a large-scale magnetic field offers a straightforward way out of this potential dilemma by decoupling these two processes: magnetic diffusivity is determined by the ionization state and composition of the disk

¹⁰ Note that in protostars that are beyond the main accretion phase L_{bol} can be expected to exceed L_{acc} (e.g., Tilling et al. 2008), which would increase the inferred value of $L_{\text{jet}}/L_{\text{acc}}$ in these sources.

¹¹ This follows from a comparison of the mass inflow speed, $\sim \nu_{\text{turb}}/R$, as inferred from the angular momentum conservation equation, with the field diffusion speed relative to the gas, $\sim \eta_{\text{turb}}/H$, as inferred from the flux conservation equation.

¹² Recent numerical simulations have indicated that the turbulent η is, in fact, of the order of the turbulent ν in disks where the turbulence derives from the magnetorotational instability (Guan & Gammie 2009; Lesur & Longaretti 2009). Note, however, that efficient inward advection of magnetic flux may nevertheless be possible in this case on account of the expected suppression of the instability near the disk surfaces (e.g., Rothstein & Lovelace 2008).

(or else by the local turbulence, if one is present) and no longer has the same underlying physical mechanism as the angular momentum transport. The disk formation models presented in Sect. 3 provide concrete examples of how open magnetic field lines can be self-consistently incorporated into a disk in which they constitute the dominant angular momentum transport channel (see also Spruit & Uzdensky 2005).

An alternative possibility is that the outflow is driven by the *stellar dynamo-generated field*. This could happen either along field lines that have been effectively severed after they penetrated the disk, as in the X-wind scenario (e.g., Shu et al. 2000), or along field lines that are still attached to the star. However, even in the latter case the outflow is envisioned to result from an interaction between the stellar magnetic field and the disk (see Sect. 5). It has also been proposed that a large-scale, open field could be generated by a *disk dynamo* (e.g., Tout & Pringle 1996; von Rekowski et al. 2003; Blackman & Tan 2004; Pudritz et al. 2007; Uzdensky & Goodman 2008). In this connection it is worth noting that, even if the disk dynamo generates small-scale, closed magnetic loops, it is conceivable, extrapolating from the situation on the Sun, that some of these loops could be dynamically extended to sufficiently long distances (in particular, beyond the respective Alfvén surfaces) for them to become effectively open (Blandford & Payne 1982).

Direct evidence for the presence of magnetic fields in either the outflow or the disk has been scant, but this may not be surprising in view of the considerable observational challenges. Among the few actual measurements are the strong circular polarization that was detected on scales of ~ 20 AU in T Tau S (Ray et al. 1997), which was interpreted as a field of at least several gauss that was advected from the origin by the associated outflow,¹³ and the meteoritic evidence that points to the presence in the protosolar nebula of a ~ 1 G field at $r \sim 3$ AU (Levy & Sonett 1978). In view of the strong indications for disk-launched outflows in FU Orionis systems, it is also worth mentioning the Zeeman-signature least-square deconvolution measurement in FU Ori (Donati et al. 2005), which was interpreted as a ~ 1 kG field (with $|B_\phi| \sim B_z/2$) originating on scales of ~ 0.05 AU in the associated disk (with the direction of B_ϕ being consistent with its origin in shearing of the vertical field by the disk differential rotation). Further support for a magnetic disk–outflow connection has been inferred from measurements of apparent rotations in a number of protostellar jets, although, as noted in Sect. 4.3 below, this evidence is still controversial.

4.3 Centrifugally Driven Winds

Our focus here is on the role of CDWs as an angular momentum transport mechanism. We survey their main characteristics and concentrate on those

¹³ Circular polarization on much larger physical scales was detected along the HH 135-136 outflow, where it was similarly interpreted as evidence for a helical magnetic field (Chrysostomou et al. 2008).

aspects that are relevant to the construction of “combined” disk/wind models, the topic of the next subsection.

Wind Equations

The qualitative basis for such outflows was considered in Sect. 2.3. In a formal treatment, the winds are analyzed using the equations of time-independent, ideal MHD.¹⁴ These equations are:

Mass conservation (continuity equation)

$$\nabla \cdot (\rho \mathbf{v}) = 0, \quad (58)$$

Momentum conservation (force equation)

$$\rho \mathbf{v} \cdot \nabla \mathbf{v} = -\nabla P - \rho \nabla \Phi + \frac{1}{4\pi} (\nabla \times \mathbf{B}) \times \mathbf{B}, \quad (59)$$

where we take the thermal pressure to be given by the perfect gas law

$$P = \frac{k_B T \rho}{\mu m_H} \quad (60)$$

(where T is the temperature, k_B is Boltzmann’s constant, μ is the molecular weight and m_H is the hydrogen atom mass),

Induction equation (magnetic field evolution)

$$\nabla \times (\mathbf{v} \times \mathbf{B}) = 0 \quad (61)$$

(cf. Eq. (20)), and the solenoidal condition (Eq. (3)). In general, one also needs to specify an *entropy conservation* equation (balance of heating and cooling). For simplicity, however, we specialize to *isothermal* flows (spatially uniform isothermal sound speed $C = \sqrt{P/\rho}$).

Generic Properties

Concentrating on *axisymmetric* flows, it is convenient to decompose the magnetic field into poloidal and azimuthal components, $\mathbf{B} = \mathbf{B}_p + \mathbf{B}_\phi$, with $\mathbf{B}_p = (\nabla A \times \hat{\phi})/r$, where the poloidal flux function $A(r, z)$ can be expressed in terms of the poloidal magnetic flux by $A = \Psi/2\pi$. The flux function is constant along \mathbf{B} ($\mathbf{B} \cdot \nabla A = 0$) and thus can be used to label the field lines. The solution of the induction equation is given by

$$\mathbf{v} \times \mathbf{B} = \nabla \chi, \quad (62)$$

¹⁴ The ideal-MHD assumption is justified by the fact that the charged particles’ drift speeds rapidly become much lower than the bulk speed as the gas accelerates away from the disk surface; see Sect. 2.4.

which shows that the electric field $\mathbf{E} = -(\mathbf{v} \times \mathbf{B})/c$ is derivable from an electrostatic potential (χ). Since $\partial\chi/\partial\phi = 0$ on account of the axisymmetry, it follows that $\mathbf{v}_p \parallel \mathbf{B}_p$. Equivalently,

$$\varrho\mathbf{v}_p = k\mathbf{B}_p, \quad (63)$$

where k is a flux-surface constant ($\mathbf{B} \cdot \nabla k = 0$, using $\nabla \cdot (\varrho\mathbf{v}) = 0$ and $\nabla \cdot \mathbf{B} = 0$). Physically, k is the *wind mass load function*,

$$k = \frac{\varrho v_p}{B_p} = \frac{d\dot{M}_w}{d\Psi}, \quad (64)$$

whose value is determined by the physical conditions near the top of the disk (more precisely, at the sonic, or slow-magnetosonic, critical surface; see discussion below). By taking the vector dot product of \mathbf{B}_p with Eq. (62) and using Eq. (63) one finds that the *field-line angular velocity* $\Omega_B = \Omega - (kB_\phi/\varrho r)$, where Ω is the matter angular velocity, is also a flux-surface constant. By writing this relation as

$$B_\phi = \frac{\varrho r}{k}(\Omega - \Omega_B) \quad (65)$$

it is seen that Ω_B can be identified with the angular velocity of the matter at the point where $B_\phi = 0$ (the disk midplane, assuming reflection symmetry).¹⁵

Using the ϕ component of the momentum conservation equation (59) and applying Eq. (63) and the field-line constancy of k , one finds that

$$l = rv_\phi - \frac{rB_\phi}{4\pi k} \quad (66)$$

is a flux-surface constant as well, representing the conserved *total specific angular momentum* (matter + electromagnetic contributions) along a poloidal field line (or streamline). In a CDW the magnetic component of l dominates over the matter component near the disk surface, $\frac{1}{\varrho v_p} \frac{r|B_p B_\phi|}{4\pi} \gg rv_\phi$, whereas at large distances this inequality is reversed. The transfer of angular momentum from the field to the matter is the essence of the *centrifugal acceleration process*. This transfer also embodies the capacity of such a wind to act as an efficient angular momentum transport mechanism. In fact, as already noted in Sect. 2.2, $rB_{z,s}B_{\phi,s}/4\pi$ represents the magnetic torque per unit area that is exerted on each surface of the disk. As was also already discussed in connection with magnetic braking, the value of $B_{\phi,s}$ is determined by the conditions outside the disk, essentially by the inertia of the matter that absorbs the transported angular momentum and exerts a back torque on the disk. In the case of a CDW, $B_{\phi,s}$ is effectively fixed by the regularity condition at the *Alfvén*

¹⁵ Eqs. (62)–(65) also hold in a nonideal fluid so long as the field remains frozen into a certain particle species (such as the electrons); in this case \mathbf{v} and Ω are replaced by the velocity and angular velocity, respectively, of that species (e.g., Königl 1989).

critical surface, which is the largest cylindrical radius from which information (carried by Alfvén waves) can propagate back to the disk. This condition yields the value of the “Alfvén lever arm” r_A , which satisfies

$$l = \Omega_B r_A^2. \quad (67)$$

The rate of angular momentum transport by the wind is thus $\sim \dot{M}_w \Omega_0 r_A^2$ (where we replaced Ω_B by the midplane value of Ω), whereas the rate at which angular momentum is advected inward by the accretion disk is $\sim \dot{M}_a \Omega_0 r_0^2$. Hence, wind transport can enable accretion at a rate

$$\dot{M}_a \simeq (r_A/r_0)^2 \dot{M}_w. \quad (68)$$

CDW solutions can have $r_A/r_0 \sim 3$ for reasonable parameters, indicating that such outflows could transport the bulk of the disk angular momentum in protostellar systems if $\dot{M}_w \simeq 0.1 \dot{M}_a$, which is consistent with the observationally inferred mass outflow rates.

By taking the vector dot product of \mathbf{B}_p with Eq. (59), one finds that the specific energy

$$\mathcal{E} = \frac{1}{2}v^2 - \frac{r\Omega_B B_\phi B_p}{4\pi\varrho v_p} + w + \Phi, \quad (69)$$

where $w = C^2 \ln(\varrho/\varrho_A)$ (with $\varrho_A = 4\pi k^2$ being the density at the Alfvén surface) is the specific enthalpy, is constant along flux surfaces. This is the *generalized Bernoulli equation*, in which the magnetic term arises from the poloidal component of the Poynting flux $c \mathbf{E} \times \mathbf{B}/4\pi$. Using Eqs. (66) and (67), this term can be rewritten as $\Omega_0 (\Omega_0 r_A^2 - \Omega r^2)$, and by approximating $\mathcal{E} \approx v_{p,\infty}^2/2$ as $r \rightarrow \infty$ and assuming that $(r_A/r_0)^2 \gg 1$, one can estimate the value of the asymptotic poloidal speed as

$$v_{p,\infty} \simeq 2^{1/2} \Omega_0 r_A, \quad (70)$$

or $v_{p,\infty}/v_K \approx 2^{1/2} r_A/r_0$. This shows that such outflows are capable of attaining speeds that exceed (by a factor of up to a few) the Keplerian speed $v_K = r_0 \Omega_0$ at their base and thus could in principle account for the measured velocities of protostellar jets.

By combining \mathcal{E} , Ω_B , and l , one can form the field-line constant

$$\mathcal{H} \equiv \mathcal{E} - \Omega_B l = \frac{1}{2}v^2 - r^2 \Omega_B \Omega + \Phi, \quad (71)$$

where we omitted w from the explicit expression. Evaluating at r_0 gives $\mathcal{H} = -\frac{3}{2}v_K^2 = -\frac{3}{2}(GM_* \Omega_0)^{2/3}$, and when this is combined with the form of \mathcal{H} at large distances (r_∞) one gets

$$r_\infty v_\phi(r_\infty) \Omega_0 - \frac{3}{2}(GM_*)^{2/3} \Omega_0^{2/3} - \frac{1}{2} [v_p^2(r_\infty) + v_\phi^2(r_\infty)] \approx 0. \quad (72)$$

If one could measure the poloidal and azimuthal speeds at a location r_∞ in a protostellar jet and estimate the central mass M_* , one would be able to

use Eq. (72) (regarded as a cubic in $\Omega_0^{1/3}$) to infer the jet launching radius $r_0 = (GM_*/\Omega_0^2)^{1/3}$ (Anderson et al. 2003). One could then also use Eqs. (65) and (67) to estimate $|B_{\phi\infty}/B_{p\infty}|$ and r_A/r_0 , respectively, and verify that they are significantly greater than 1, as required for self-consistency. This has already been attempted in several instances, where it was claimed that the results are consistent with a disk-driven outflow that originates on scales $\gtrsim 1$ AU and carries a significant fraction of the disk angular momentum (e.g., Ray et al. 2007; Coffey et al. 2007; Chrysostomou et al. 2008). However, the interpretation of the measurements has been controversial (e.g., Soker 2005; Cerqueira et al. 2006) and there have been some conflicting observational results (e.g., Cabrit et al. 2006), so the issue is not yet fully settled.

Critical Points of the Outflow

The critical points occur in stationary flows at the locations where the fluid velocity equals the speed of a backward-propagating disturbance. Since the disturbances propagate along the characteristics of the time-dependent equations, the critical points can be regarded as relics of the initial conditions in a time-dependent flow (Blandford & Payne 1982). If one takes the magnetic field configuration as given and considers the poloidal flow along \mathbf{B}_p , one can derive the location of the critical points and the values of the critical speeds (i.e., the values of v_p at the critical points) by regarding the Bernoulli integral as a function of the spatial coordinate along the field line and of the density ($\mathcal{H} = \mathcal{H}(s, \varrho)$, where s is the arc-length of the streamline) and deriving the extrema of \mathcal{H} by setting $\partial\mathcal{H}/\partial\varrho = 0$ (which yields the critical speeds) and $\partial\mathcal{H}/\partial s = 0$ (which, together with the other relation, yields the critical point locations). The critical points obtained from the generalized Bernoulli equation (69) correspond to v_p becoming equal to either the slow- or the fast-magnetosonic wave speeds (e.g., Sakurai 1985). In the full wind problem, the shape of the field lines must be determined as part of the solution by solving also the transfield (or Grad-Shafranov) equation, which involves the force balance *across* the flux surfaces. This equation introduces a critical point corresponding to $v_p = v_{Ap}$ (Okamoto 1975). However, the critical points of the *combined Bernoulli and transfield equations* are in general *different* from those obtained when these two equations are solved separately. The *modified* slow, Alfvén, and fast points occur on surfaces that correspond to the so-called *limiting characteristics* (or separatrices; e.g., Tsinganos et al. 1996; Bogovalov 1997). The relevance of the modified critical points has been recognized already in the original radially self-similar CDW model constructed by Blandford & Payne (1982). The modified critical surfaces of the exact, semianalytic wind solutions obtained in this model are defined by the locations where the component of the flow velocity that is perpendicular to the directions of axisymmetry (i.e., $\hat{\phi}$) and self-similarity (i.e., the spherical radius vector $\hat{\mathbf{R}}$) equals the MHD wave speed in that direction (the $\hat{\theta}$ direction, using spherical coordinates $\{R, \theta, \phi\}$). The significance of the modified fast surface, which in

general is located beyond its classical counterpart, is that the poloidal acceleration of the wind continues all the way up to it: initially (roughly until the flow reaches the Alfvén surface) the acceleration is primarily centrifugal, but further out the pressure gradient of the azimuthal field component comes to dominate.

Example: the slow-magnetosonic critical surface

This critical surface is relevant to the determination of the mass flux in a disk-driven wind. There is some uncertainty about this case since the location of the first critical point is typically very close to the disk surface (with $|z|$ being $\ll r$), so a priori it is not obvious that ideal MHD is already a good approximation there. Under nonideal MHD conditions, all magnetic terms in a disturbance are formally wiped out by magnetic diffusivity on its backward propagation from “spatial infinity,” and one is left with pure sound waves (e.g., Ferreira & Pelletier 1995). Here we discuss the situation where the critical point is encountered when the charged particles’ drift speeds are already small enough in comparison with the bulk speed to justify employing ideal MHD. In this case the poloidal flow is parallel to the poloidal magnetic field (see Eq. (63)) and the relevant wave speed is the slow-magnetosonic (sms) one. We consider the standard (rather than the modified) sms point, and our explicit derivation can hopefully serve to correct inaccurate statements that have appeared in some of the previous discussions of this topic in the literature.

In the magnetically dominated region above the disk surface the shape of the field lines changes on the scale of the spherical radius R . Anticipating that the height z_{sms} of the sms point is $\ll R$, we approximate the shape of the field line just above the point $\{r_s, z_s\}$ on the disk surface by a straight line (cf. Sect. 2.3):

$$r = r_s + s \sin \theta_s, \quad z = z_s + s \cos \theta_s, \quad (73)$$

where the angle θ_s gives the field-line inclination at the disk surface ($\sin \theta_s = B_{r,s}/B_{p,s}$; $\tan \theta_s = B_{r,s}/B_z$). The Bernoulli integral (in the form of Eq. (71)) then becomes, after substituting $\Phi = -GM_*/(r^2 + z^2)^{1/2}$,

$$\begin{aligned} \mathcal{H}(s, \varrho) = & \frac{k^2 B_p^2}{2\varrho^2} + \frac{\Omega_B^2}{2} (r_s + s \sin \theta_s)^2 \left(\frac{\Omega}{\Omega_B} \right) \left(\frac{\Omega}{\Omega_B} - 2 \right) \\ & - \frac{GM_*}{[(r_s + s \sin \theta_s)^2 + (z_s + s \cos \theta_s)^2]^{1/2}} + C^2 \ln \left(\frac{\varrho}{\varrho_A} \right), \quad (74) \end{aligned}$$

where $\Omega(s, \varrho)$ is given by combining

$$\Omega = \frac{1 - \frac{r_A^2 \varrho_A}{r^2 \varrho}}{1 - \frac{\varrho_A}{\varrho}} \Omega_B \quad (75)$$

(obtained from Eqs. (65)–(67)) and Eq. (73). In the hydrostatic approximation to the disk structure (see Sect. 4.4) $\Omega_B = \Omega_K(r_s)$. We expect this equality to

hold approximately also for the exact solution, in which $v_z \neq 0$, so that, in particular, $\Omega_B \approx \Omega$ in the region of interest.

Setting $\partial\mathcal{H}/\partial\varrho = 0$ yields the speed of an sms wave propagating along $\hat{\mathbf{B}}_p$:

$$v_{\text{sms}} = \frac{B_{p,s}}{B_s} C, \quad (76)$$

where $B_s = (B_{p,s}^2 + B_{\phi,s}^2)^{1/2}$ and we approximated $(B_{p,\text{sms}}/B_{\text{sms}})^2$ by $(B_{p,s}/B_s)^2$ and assumed $\varrho/\varrho_A \gg 1$ and $(\Omega/\Omega_B - 1)^2 \approx (r_A/r)^4 (\varrho_A/\varrho)^2 \ll 1$ in the region between the top of the disk and the sms surface. Setting also $\partial H/\partial r = 0$ and approximating $r_{\text{sms}} \approx r_s$ then gives the height of this point:

$$\frac{z_{\text{sms}}}{z_s} = \frac{3 \tan^2 \theta_s}{3 \tan^2 \theta_s - 1}. \quad (77)$$

Equation (77) yields a meaningful result only if $\tan \theta_s > 1/\sqrt{3}$, i.e., if the field line is inclined at an angle $> 30^\circ$ to the z axis. This is the CDW launching condition in a Keplerian disk (Eq. (6)) that was derived in Sect. 2.3 using the mechanical analogy to a “bead on a rigid wire.” The relationship between these two derivations becomes clear when one notes that, in the limit $(\Omega/\Omega_B - 1)^2 \ll 1$, the 2nd term on the right-hand side of Eq. (74) becomes equal to the centrifugal potential $-\Omega^2 r^2/2$, so that the 2nd and 3rd terms (which together dominate the right-hand side of this equation) are just the effective potential Φ_{eff} used in Eq. (5).¹⁶ The correspondence of the sms point to the maximum of Φ_{eff} was already noted in Sect. 2.3.

The density at the sms point can be related to the density at the disk surface by evaluating the energy integral (74) at both z_s and z_{sms} . This yields

$$\frac{\varrho_{\text{sms}}}{\varrho_s} = \exp \left\{ -\frac{1}{2} - \frac{1}{2} \left(\frac{z_s \Omega_K(z_s)}{C} \right)^2 \frac{1}{3 \tan^2 \theta_s - 1} \right\}, \quad (78)$$

where we assumed $(v_{p,s}/v_{\text{sms}})^2 \ll 1$. The mass flux injected into the wind from the two sides of the disk is then

$$\frac{1}{2\pi r} \frac{d\dot{M}_w}{dr} = 2\varrho_{\text{sms}} v_{\text{sms}} \cos \theta_s = 2\varrho_{\text{sms}} C \frac{B_z}{B_s} \quad (79)$$

(e.g., Lovelace et al. 1995).

When θ_s approaches (and decreases below) 30° the field-line curvature needs to be taken into account in the analysis. The height of the sonic point rapidly increases to $\sim R$, with the potential difference growing to $\sim GM_*/R$: the launching problem becomes essentially that of a thermally driven spherical wind (e.g., Levinson 2006).

¹⁶ Furthermore, the condition $\partial\mathcal{H}/\partial r = 0$ is equivalent to $\mathbf{B}_p \cdot \nabla \Phi_{\text{eff}} = 0$ in this limit (Campbell 2002), so the latter relation can also be used to obtain the location of the sms point in this case (e.g., Ogilvie 1997).

It has been argued (Spruit 1996) that the field-line inclination increases systematically with radius along the disk surface and that only in a narrow radial range the conditions are favorable for driving a wind that both satisfies the CDW launching condition and is not “overloaded” (and hence conceivably highly unstable; cf. Cao & Spruit 1994). This is an intriguing suggestion, given the fact that so far there is no observational evidence for an extended wind-driving region in protostellar disks (see Sect. 4.1). However, in principle it may be possible to launch outflows over a large radial range. In particular, as illustrated by the similarity solution presented in Sect. 3, if the magnetic flux is advected inward by the accretion flow, the field-line inclination could be favorable for launching and need not change strongly along the disk. Furthermore, evidently the mass loading of stable disk/wind configurations actually *decreases* as θ_s is increased (see Sect. 4.5).

Exact Wind Solutions

As was already noted in Sect. 2.5, the radial self-similarity approach has been used to construct exact global solutions of CDWs. The basic character of this model is revealed by the prototypal Blandford & Payne (1982) solution. The underlying assumption that all quantities scale as a power law of the spherical radius implies that all the critical surfaces are conical. Furthermore, all the relevant speeds (including the fluid, sound, and Alfvén) must scale like the characteristic speed of the problem (v_K), i.e., as $R^{-1/2}$. The scaling of the magnetic field amplitude can be inferred from the vertically integrated thin-disk equations presented in Sect. 3.2, in which we now set $\partial/\partial t \equiv 0$. In particular, if the mass outflow from the disk has only a negligible effect on the accretion rate then $\dot{M}_a = 2\pi r|v_r|\Sigma = \text{const}$ by Eq. (31) and the angular momentum conservation equation (33) in a Keplerian disk can be written as

$$\frac{1}{2}\dot{M}_a v_K = r^2 |B_z B_{\phi,s}|. \quad (80)$$

Equation (80) implies the similarity scaling $B \propto r^{-5/4}$, from which we infer by dimensional arguments ($v_A \propto B/\sqrt{\varrho}$) that $\varrho \propto r^{-3/2}$ in this case. It then follows that $\dot{M}_w \propto \ln r$ (cf. Eq. (79)), which is consistent with the underlying assumption that only a small fraction of the inflowing mass leaves the disk over each decade in radius. More generally, one can define a mass *ejection index* $\xi > 0$ by

$$\xi \equiv \frac{d \ln \dot{M}_a}{d \ln r} \quad (81)$$

(e.g., Ferreira & Pelletier 1995) and deduce

$$\frac{d \ln B}{d \ln r} = \xi - \frac{5}{4}, \quad \frac{d \ln \varrho}{d \ln r} = \xi - \frac{3}{2} \quad (82)$$

(e.g., Contopoulos & Lovelace 1994), with $\xi \rightarrow 0$ corresponding to the Blandford & Payne (1982) solution.¹⁷ The poloidal electric current scales as $I \propto rB_\phi \propto r^{(2\xi-1)/4}$. For $\xi > 1/2$ the flow is in the current-carrying regime, with the poloidal current density being antiparallel to the magnetic field. In this case the current tends to zero as the symmetry axis is approached, so such solutions should provide a good representation of the conditions near the axis of a highly collimated flow. Conversely, solutions with $\xi < 1/2$ correspond to the return-current regime (in which the poloidal current density is parallel to the field) and are most suitable at larger cylindrical distances. The Blandford & Payne (1982) solution is sometimes critiqued for having a singular behavior on the axis.¹⁸ One should bear in mind, however, that even though the detailed global current distribution (which includes both a current-carrying and return-current regimes) cannot be represented by the simplified self-similar solution, this flaw is not fundamental. Besides, given that the disk has a finite inner radius, the issue of the behavior of the flow at $r = 0$ is, to a certain degree, merely academic. Whereas the value of the ejection index is arbitrary in pure wind models, it becomes an eigenvalue of the self-similar solution (fixed by the regularity condition at the sonic, or sms, critical surface; see Sect. 4.3) when one considers a “combined” disk/wind model (e.g., Li 1996a).

While the magnetic field lines must bend away from the symmetry axis within the disk in order to satisfy the wind launching condition (6) at the surface, as soon as the magnetically dominated region at the base of the wind is reached they start to bend back toward the axis on account of the magnetic tension force (see Sect. 2.1). Further collimation is achieved in current-carrying jets by the *hoop stress* of the toroidal magnetic field (the term $-J_z B_\phi / c = -(1/8\pi r^2)\partial(rB_\phi)^2/\partial r$ in the radial force equation), the analog of a z-pinch in laboratory plasma experiments. The asymptotic behavior in general depends on the current distribution: if $I \rightarrow 0$ as $r \rightarrow \infty$ then the field lines are space-filling paraboloids, whereas if this limit for the current is finite then the flow is collimated to cylinders (e.g., Heyvaerts & Norman 1989). In practice, however, self-similar wind solutions typically do not reach the asymptotic regime but instead self-focus (with streamlines intersecting on the axis) and terminate at a finite height (e.g., Vlahakis et al. 2000).

The cold self-similar wind solutions are specified by any two of the following three parameters:

¹⁷ Interestingly, one can also generalize the Blandford & Payne (1982) solution to a class of semianalytic, but *non*-self-similar solutions, defined by the constancy of a certain function of the magnetic flux that controls the shape of the Alfvén surface (Pelletier & Pudritz 1992). The Blandford & Payne solution then separates wind configurations in which the initial field-line inclination increases progressively with radius from outflows that emerge from a bounded region and in which the initial field inclination decreases with r and the field lines converge into a cylindrical sheath.

¹⁸ It is in fact a double singularity, since on the axis itself there is an oppositely directed line current that exactly compensates for the distributed return current.

$$\begin{aligned}
\lambda &\equiv \frac{l}{v_{\text{Ks}} r_s} && \text{normalized specific angular momentum} \\
\kappa &\equiv k \frac{v_{\text{Ks}}}{B_{z,s}} && \text{normalized mass/magnetic flux ratio} \\
b_{r,s} &\equiv \frac{B_{r,s}}{B_{z,s}} && \text{poloidal field inclination at the disk surface ,}
\end{aligned} \tag{83}$$

where $b_{r,s}$ must satisfy the constraint (6). A viable solution is further characterized by $\lambda > 1$ (typically $\gg 1$) and $\kappa < 1$ (typically $\ll 1$). A two-parameter choice yields a solution if the corresponding flow crosses the modified Alfvén critical surface (see Sect. 4.3); if the two parameters are κ and λ then, for any given value of κ , this can happen only if λ exceeds a minimum value that approximately satisfies $\kappa \lambda_{\text{min}} (\lambda_{\text{min}} - 3)^{1/2} = 1$.¹⁹ In Sect. 4.4 we discuss joining a global wind solution of this type to a radially localized wind-driving disk solution. In this case the sonic (or sms) critical-point constraint imposed on the latter solution yields the value of κ , and, in turn, the Alfvén critical-point constraint on the wind solution fixes one of the disk model parameters (for example, by providing the value of $B_{\phi,s}/B_{z,s} = -\kappa(\lambda - 1)$ from given values of κ and $b_{r,s}$).²⁰

Observational Implications

The exact wind solutions and estimates of the physical conditions around young stellar objects make it possible to identify a number of physical characteristics of disk-driven protostellar winds that could have potentially significant observational implications. While this topic is not directly within the scope of this book, we nevertheless briefly describe some of these properties here inasmuch as it may not always be feasible in practice to distinguish between the observational signatures of a disk and a wind. Furthermore, invoking a disk-driven wind may sometimes provide a straightforward explanation to a disk observation that may otherwise seem puzzling. Besides the references explicitly listed below, the reader may also consult the review articles by Königl & Ruden (1993) and Königl & Pudritz (2000) on this subject.

Centrifugal driving is found to be an efficient acceleration mechanism, leading to a rapid increase in the poloidal speed, and a correspondingly strong decrease in the wind density, above the disk surface (see Fig. 4).²¹ This leads

¹⁹ This expression differs slightly from the one that appeared in Blandford & Payne (1982).

²⁰ Although self-similar CDW solutions in which the wind passes also through the fast-magnetosonic critical surface have been obtained, the implications of this additional constraint to a global disk/wind model remain unclear. Ferreira & Casse (2004), for instance, suggested that in order to cross this surface the outflow must experience significant heating after it leaves the disk and that the added constraint is related to this requirement.

²¹ The model wind presented in Fig. 4 exhibits a comparatively weak collimation. The degree of collimation depends on the model parameters and is particularly

to a strong stratification, which, in fact, is most pronounced in the \hat{z} direction even in the R -self-similar wind models (Safier 1993b). The strong momentum flux in the wind also implies that an outflow originating from beyond the *dust sublimation radius* could readily uplift dust from the disk (Safier 1993a). This may lead to viewing angle-dependent obscuration and shielding of the central continuum, whose effect would be distinct from that of molecular cloud gas undergoing gravitational collapse.²² The stratified dust distribution could intercept a large portion of the central continuum radiation and reprocess it to the infrared, which could be relevant to the interpretation of the IR spectra of low- and intermediate-mass star/disk systems (e.g., Königl 1996; Tambovtseva & Grinin 2008). Furthermore, scattering by the uplifted dust could contribute to the observed polarization pattern in these objects.²³

Although, as we already noted, ideal MHD should be an excellent approximation for modeling the *dynamics* of the flow (except perhaps right above the disk surface, where the nonideal formalism employed within the disk might still be relevant for determining the first critical point of the wind), the estimated degree of ionization at the base of a protostellar disk wind is typically low enough that energy dissipation induced by ion-neutral drag (ambipolar diffusion) could play an important role in the wind *thermodynamics*. This is because the volumetric heating rate scales as $|(\nabla \times \mathbf{B}) \times \mathbf{B}|^2 / \gamma_i \varrho_i \varrho \propto 1 / \gamma_i \varrho_i$ (see Sect. 2.4), where the distributions of \mathbf{B} and ϱ are regarded as being fixed by the flow dynamics, whereas adiabatic cooling, the most important temperature-lowering mechanism, remains relatively inefficient in a collimated disk outflow. Under these circumstances, the temperature might rise rapidly (Safier 1993a), although its precise terminal level depends on the relevant value of the collisional drag coefficient γ_i (Shang et al. 2002). This heating mechanism could contribute to the observed forbidden line emission (Safier 1993b; Cabrit et al. 1999; Garcia et al. 2001a,b) and thermal radio emission (Martin 1996) from CTTs, although in both of these applications an additional source of heating might be needed, possibly associated with dissipation of weak shocks and turbulence (e.g., O’Brien et al. 2003; Shang et al. 2004).

On large scales, centrifugally driven outflows assume the structure of a collimated jet (most noticeable in the density contours) and a surrounding wide-angle wind (Shu et al. 1995; Li 1996b). This bears directly on the general morphology of protostellar sources, and in particular on the shapes of the (wind/jet)-driven outflow lobes that form in the surrounding molecular gas.

sensitive to the mass loading of the outflow (e.g., Pudritz et al. 2007). Protostellar jets are inferred to correspond to more highly collimated disk winds, in which the enhanced mass loading might be attributed to the presence of a disk corona (e.g., Dougados et al. 2004).

²² In an application to active galactic nuclei, this effect was invoked by Königl & Kartje (1994) to account for the obscuring/absorbing “molecular torus” identified in the centers of Seyfert galaxies.

²³ For an application of this model to the polarization properties of Seyfert galaxies, see Kartje (1995).

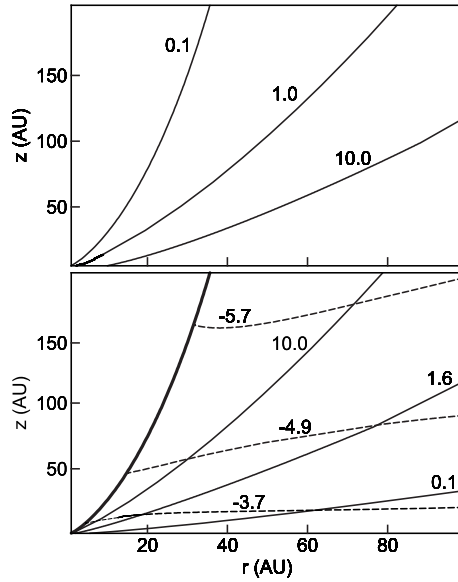


Fig. 4. Structure of a Blandford-Payne-type self-similar CDW from a protostellar disk (model C in Safer 1993a). **Top:** Meridional projections of the streamlines (labeled by the value, in AU, of the radius where they intersect the disk). **Bottom:** Contours of $v_{p,\infty}/v_{K1}$ (*solid lines*), where $v_{p,\infty}$ is the asymptotic poloidal speed and v_{K1} is the Keplerian speed at 1 AU, and of $\log(\varrho/\varrho_1)$ (*dashed lines*), where ϱ_1 is the density at the base of the wind at 1 AU. The heavy line on the left indicates the streamline that originates at 0.1 AU.

4.4 Equilibrium Disk/Wind Models

In contrast with the wind zone, where the dynamics is well described by an effectively infinite conductivity, the accretion disk in protostellar systems must be modeled using nonideal MHD. The structure of the accretion flow thus depends critically on the properties of the conductivity tensor at each point, which are in turn determined by the spatial distribution of the degree of ionization (see Eqs. (12)–(14)). We therefore start this subsection by reviewing the physical processes that affect the disk ionization (see also Chap. II [The Chemical Evolution of Protoplanetary Disks]), which would allow us to choose the relevant physical parameters for our models. In reality the accretion flow itself has an influence on the ionization structure — through its effect on the disk column density (see Sect. 2.4) or on the distribution of dust grains (see Sect. 6), for example — which a truly self-consistent model must take into account. So far only simpler models have been constructed, in which this influence is not fully accounted for and a variety of approximations are employed. We discuss these models next, describing the basic properties of the

derived equilibrium solutions and distinguishing between “strongly coupled” and “weakly coupled” disk configurations.

Disk Ionization Structure

The dependence of the degree of field–matter coupling on the abundances of the ionized species in the disk (ions, electrons and charged dust grains) is a direct outcome of the fact that this coupling is effected by the collisions of these particles with the much more abundant neutrals. The degree of ionization is given by the ratio of the sum of the positively (or, equivalently, negatively) charged particle densities to the neutral particle density. It is calculated by balancing the ionization and recombination processes operating in the disk.

Interstellar (and possibly also protostellar) cosmic rays as well as X-ray and far-UV radiation produced by the magnetically active protostar (e.g., Glassgold et al. 2000, 2005) are the main potential ionizing agents in protostellar environments. It is, however, unclear how effective cosmic-ray ionization really is, since the low-energy particles most relevant for this purpose may be deflected by magnetized disk or stellar outflows or by magnetic mirroring near the disk surface, and they might also be scattered by magnetic turbulence within the disk. If present, they may be more important than X-rays in the inner disk ($r \lesssim 1$ AU), where the surface density is larger than the X-ray attenuation length. But if cosmic rays are excluded from this region and ionized particles are not transported there by other means (e.g., Turner et al. 2007), the gas near the midplane might be ionized only at the low rate of decay of radioactive elements such as ^{40}K . On the other hand, free electrons are rapidly lost through recombination processes that occur both in the gas phase (where electrons recombine with molecular and metal ions via dissociative and radiative mechanisms, respectively) and on grain surfaces, and through sticking to dust particles (e.g., Oppenheimer & Dalgarno 1974; Nishi et al. 1991). The ionization equilibrium is, however, very sensitive to the abundance of metal atoms, as they rapidly remove charges from molecular ions but then recombine much more slowly with electrons (e.g., Sano et al. 2000; Fromang et al. 2002).

Dust grains can also significantly affect the degree of field–matter coupling if they are mixed with the gas. They do so in two ways. First, they reduce the ionization fraction by absorbing charges from the gas and by providing additional recombination pathways for ions and electrons. Second, in high-density regions the grains themselves can become an important charged species (e.g., Nishi et al. 1991), leading to a reduction in the magnetic coupling because grains have much smaller Hall parameters than the much less massive electrons and ions. We note in this connection that, if dust grains settle to the midplane, the ionization fraction may become sufficiently large to provide adequate magnetic coupling even in the inner ($\lesssim 1$ AU) disk regions (Wardle 2007). This conclusion could, however, be mitigated in the presence of turbulence, which might leave a residual population of small dust grains (carrying

a significant fraction of the total grain charge) suspended in the disk (e.g., Nomura & Nakagawa 2006; Natta et al. 2007).

Exact Disk Solutions

To gain physical insight into the distinguishing properties of wind-driving disks, we consider a simplified model originally formulated by Wardle & Königl (1993). In this model, the entire angular momentum of the accreted matter is assumed to be transported by a CDW. The disk is taken to be geometrically thin, vertically isothermal, stellar gravity-dominated, and threaded by an open magnetic field (possessing reflection symmetry about the midplane). Under the thin-disk approximation, the vertical magnetic field component is taken to be uniform with height in the disk solution. The disk gas is assumed to be in the ambipolar diffusivity regime, with ions and electrons being the dominant charge carriers. In the original model, the ion density was taken to be constant with height (which could be a reasonable approximation in the outer regions of certain real systems). The main simplifications involve considering only a *radially localized* ($\Delta r \ll r$) disk region and (in accord with the thin-disk approximation) retaining the z derivatives but neglecting all r derivatives except those of v_ϕ (which scales as $r^{-1/2}$) and B_r (which appears in $\nabla \cdot \mathbf{B} = 0$). The neglect of the radial derivatives in the mass conservation equation (Eq. (58)) implies that the vertical mass flux ρv_z is taken to be uniform with height in the disk solution.²⁴ This solution is extended through the first critical point (which is the thermal sonic point if the flow is still diffusive and the sms point if it is already in the ideal-MHD regime; see Sect. 4.3) and then matched onto a *global* Blandford & Payne (1982) ideal-MHD wind solution. These simplifications do not compromise the physical essence of the results. In particular, the qualitative characteristics remain unchanged when the radially localized disk solution is generalized to a global configuration in which both the disk and the wind are described by a single self-similar model that includes both z and r derivatives (e.g., Li 1996a). Furthermore, solutions with similar properties are obtained when the disk is in the Hall or Ohm diffusivity regimes (e.g., Salmeron et al. 2010) and when the full conductivity tensor is used in conjunction with a realistic ionization profile (see Fig. 5).

²⁴ This approximation has been critiqued (e.g., Ferreira 1997) for not allowing v_z to assume negative values within the disk, as it must do in cases (expected to be typical) in which the disk thickness decreases as the protostar is approached. This issue can be fully addressed only in the context of a global disk/wind model. However, it can be expected that any error introduced by this approximation would be minimized if the upward mass flux remained small enough for v_z to have only a weak effect on the behavior of the other variables within the disk. Under the assumption that $|v_r|$ is of the same order of magnitude as $|v_\phi - v_K|$ one can readily show that the condition for this to hold is that v_z/C remain $\ll 1$ everywhere within the disk. This can be checked a posteriori for each derived solution.

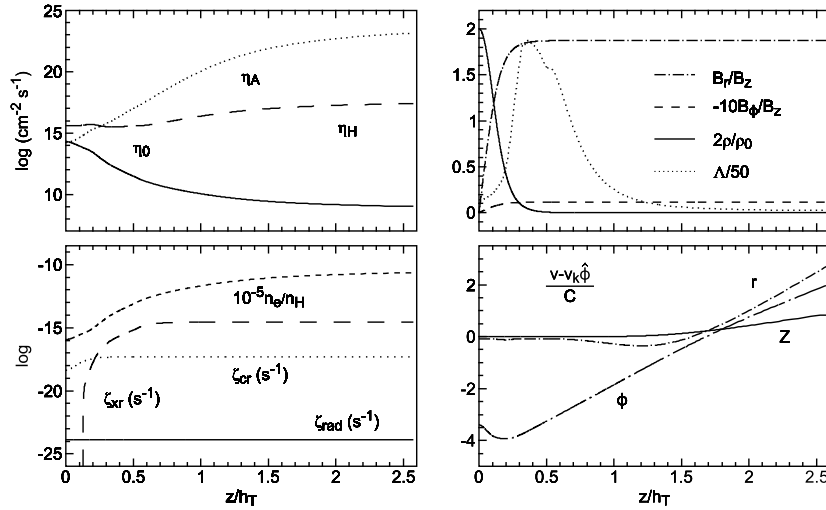


Fig. 5. Vertical structure of a radially localized wind-driving disk solution at 1 AU around a Sun-like protostar. The disk is assumed to have a column density of $\Sigma = 600 \text{ g cm}^{-2}$ and its model parameters are $a_0 = 0.75$, $C/v_K = 0.1$, $\epsilon = 0.1$, and $\epsilon_B = 0$. The parameters of the matched radially self-similar CDW are $\kappa = 2.6 \times 10^{-6}$, $\lambda = 4.4 \times 10^3$, and $b_{r,s} = 1.6$. **(Left) Top:** Ambipolar, Hall, and Ohm diffusivities. **Bottom:** Ionization rates by cosmic rays (**cr**), X-rays (**xr**), and radioactivity (**rad**), and electron fraction n_e/n_H . **(Right) Top:** Radial and azimuthal magnetic field components, mass density, and Elsasser number. **Bottom:** Velocity components. The mass accretion rate for this model is $7 \times 10^{-6} M_\odot \text{ yr}^{-1}$, which is consistent with the inferred values for the early (Class 0/Class I) protostellar accretion phase.

In general, an equilibrium disk solution is specified by the following parameters:

1. $a_0 \equiv v_{A0}/C$, the midplane ratio of the Alfvén speed (based on the uniform vertical field component) to the sound speed. This parameter measures the magnetic field strength.²⁵
2. C/v_K , which in a thin isothermal disk is equal to h_T/r , the ratio of the tidal (i.e., reflecting the vertical gravitational compression) density scale height to the disk radius. While this parameter, which measures the geometric thinness of the disk, does not appear explicitly in the normalized structure equations, it nevertheless serves to constrain physically viable solutions (see Eq. (84) below).
3. The midplane ratios of the conductivity tensor components: $[\sigma_P/\sigma_\perp]_0$ (or $[\sigma_H/\sigma_\perp]_0$) and $[\sigma_\perp/\sigma_O]_0$. They characterize the conductivity regime of the gas (see Sect. 2.4). When there are only two charged species (ions

²⁵ Note that a_0 is related to the midplane plasma beta parameter β_0 through $a_0 = (2/\gamma\beta_0)^{1/2}$, where γ denotes the adiabatic index of the fluid.

and electrons), one can equivalently specify the midplane Hall parameters β_{i0} and β_{e0} . In the inner disk regions the conductivity tensor components typically vary with height, reflecting the ionization structure of the disk (see Fig. 5).

4. The midplane Elsasser number A_0 (see Eqs. (23) and (25)), which measures the degree of coupling between the neutrals and the magnetic field.
5. $\epsilon \equiv -v_{r,0}/C$, the normalized inward radial speed at the midplane. Although the value of ϵ could in principle be negative (as, in fact, it is in certain viscous disk models; e.g., Takeuchi & Lin 2002), it is expected to remain > 0 when a large-scale magnetic field dominates the angular momentum transport.
6. $\epsilon_B \equiv -v_{B_r,0}/C$, the normalized radial drift speed of the poloidal magnetic field lines (see Eq. (22)). This parameter vanishes in a strictly steady-state solution but is nonzero if, as expected, the magnetic field lines drift radially on the “long” accretion time scale $r/|v_r|$. It is incorporated into the model through the z component of Eq. (20) (i.e., one sets $\partial B_z/\partial t \neq 0$ but keeps $\partial B_r/\partial t = 0$ and $\partial B_\phi/\partial t = 0$).²⁶

We already remarked in Sect. 4.3 on how the wind solution, through the Alfvén-surface regularity condition, can be used to constrain the disk solution when the two are matched. In particular, if the disk solution is used to fix the wind parameters κ (through the sonic/sms critical-point constraint) and $b_{r,s}$, the wind solution yields $B_{\phi,s}/B_z$, which in turn can be used to obtain the value of the disk parameter ϵ . Previous “combined” disk/wind models treated ϵ_B as a free parameter and typically set it equal to zero.²⁷ Under this approach, $b_{r,s}$ was fully determined by the conditions inside the disk. However, as we noted in Sect. 3.2 (see also Ogilvie & Livio 2001), $b_{r,s}$ is in fact also determined by the conditions outside the disk and can be directly related to the distribution of B_z along the disk if the force-free field above the surface can be adequately approximated as being also current free (see Eq. (40)). In

²⁶ It is worth noting, though, that the poloidal components of Eq. (20) can be written as $\partial\Psi/\partial t = -2\pi r B_0 v_{B_r,0}$, with $B_z = (1/2\pi r)\partial\Psi/\partial r$ and $B_r = -(1/2\pi r)\partial\Psi/\partial z$. Thus, if B_z changes because of the slow radial diffusion of the flux surfaces, so will also B_r . However, it can be argued (Königl et al. 2010) that B_r (and similarly also B_ϕ) can in principle change at any given radial location on the much shorter dynamical time r/v_ϕ through field-line shearing by the local velocity field. One can therefore assume that B_r and B_ϕ attain their equilibrium configurations on the “short” time scale and neglect, in comparison, the much slower variations that are expressed by the explicit time derivative terms. The B_z component is distinct in that it can only change on the “long” radial drift time.

²⁷ Wardle & Königl (1993) noted, however, that for physical consistency one has to require $\epsilon_B < \epsilon$. They also demonstrated that the solution variables (except for $B_{\phi,s}$ and $v_{r,0}$) are insensitive to the value of this parameter, as expected from the fact that the only modification to the equations introduced by varying ϵ_B involves changing the radial velocity of the reference frame in which the poloidal field lines are stationary.

a more general treatment of the disk/wind problem, this constraint can be used to fix the value of ϵ_B (see Teitler 2010).

Before turning to the specific solution displayed in Fig. 5, it is instructive to list the dominant magnetic terms (under the thin-disk approximation) in the neutrals’ force equation (Eq. (59)) and review their main effects inside the disk. We have (see Eqs. (28)–(30)):

- *radial* component: $\frac{B_z}{4\pi} \frac{dB_r}{dz}$
representing the magnetic tension force that acts in opposition to central gravity;
- *azimuthal* component: $\frac{B_z}{4\pi} \frac{dB_\phi}{dz}$
representing the magnetic torque that transfers angular momentum from the matter to the field;
- *vertical* component: $-\frac{d}{dz} \frac{B_r^2 + B_\phi^2}{8\pi}$
representing the magnetic squeezing of the disk (which acts in the same direction as the gravitational tidal force and in opposition to the thermal pressure-gradient force).

The solution shown in Fig. 5 describes the vertical structure of a disk that changes from being Hall-dominated near the midplane to being ambipolar-dominated near the surface. While the qualitative properties of the solution are not sensitive to the details of the diffusivity profile, it is heuristically useful to consider a distinct diffusivity regime. We therefore specialize in the following discussion to the “pure ambipolar” (with $\varrho_i(z) = \text{const}$) case treated in Wardle & Königl (1993). As illustrated in Fig. 6 (in which it is assumed that $\epsilon_B = 0$), the disk can be vertically divided into three distinct zones:²⁸ a quasi-hydrostatic region near the midplane, where the bulk of the matter is concentrated and most of the field-line bending takes place, a transition zone where the inflow gradually diminishes with height, and an outflow region that corresponds to the base of the wind. The first two regions are characterized by a radial inflow and sub-Keplerian rotation, whereas the gas at the base of the wind flows out with $v_\phi > v_K$.

- The *quasi-hydrostatic region* is matter dominated, with the ionized particles and magnetic field being carried around by the neutral material. The ions are braked by a magnetic torque, which is transmitted to the neutral gas through the frictional drag; therefore $v_{i\phi} < v_\phi$ in this region. The neutrals thus lose angular momentum to the field, and their back reaction leads to a buildup of the azimuthal field component away from the midplane. The loss of angular momentum enables the neutrals to drift toward the center, and in doing so they exert a radial drag on the field lines. This drag must be balanced by magnetic tension, so the field lines bend away from the rotation axis. This bending builds up the ratio B_r/B_z , which

²⁸ Our discussion pertains to disks in which $\Lambda > 1$ throughout their entire vertical extent, but is also applies to the $\Lambda > 1$ wind-driving surface layers of “weakly coupled” disks.

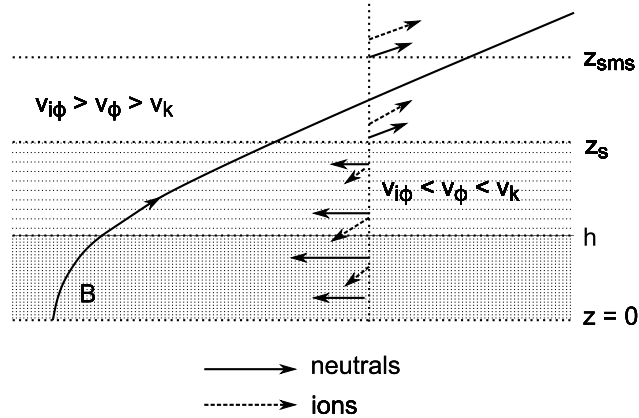


Fig. 6. Schematic diagram of the vertical structure of an ambipolar diffusion-dominated disk, showing a representative field line and the poloidal velocities of the neutral and the ionized gas components. Note that the poloidal velocity of the ions vanishes at the midplane ($z = 0$), consistent with the assumption that $\epsilon_B = 0$, and that it is small for both components at the top of the disk ($z = z_s$). The relation between the azimuthal speeds is also indicated.

needs to exceed $1/\sqrt{3}$ at the disk surface to launch a centrifugally driven wind. The magnetic tension force, transmitted through ion–neutral collisions, contributes to the radial support of the neutral gas and causes it to rotate at sub-Keplerian speeds.

- The growth of the radial and azimuthal field components on moving away from the midplane results in a magnetic pressure gradient that tends to compress the disk. The magnetic energy density comes to dominate the thermal and gravitational energy densities as the gas density decreases, marking the beginning of the *transition zone* (at $z \approx h$, where h is the density scale height). The field above this point is nearly force free and locally straight (see Sects. 2.1 and 2.3).
- The field angular velocity Ω_B is a flux-surface constant (see Eq. (65) and footnote 15; note, however, that this strictly holds only when ϵ_B is identically zero). The ion angular velocity $v_{i\phi}/r$ differs somewhat from Ω_B but still changes only slightly along the field. Since the field lines bend away from the symmetry axis, the cylindrical radius r , and hence $v_{i\phi}$, increase along any given field line, whereas v_ϕ decreases because of the near-Keplerian rotation law. Eventually a point is reached where $(v_{i\phi} - v_\phi)$ changes sign. At this point the magnetic stresses on the neutral gas are small and its angular velocity is almost exactly Keplerian.²⁹ Above this

²⁹ This result was utilized in the derivation of the slow-magnetosonic critical surface properties in Sect. 4.3.

point the field lines overtake the neutrals and transfer angular momentum back to the matter, and the ions start to push the neutrals out in both the radial and the vertical directions. This region can be regarded as the *base of the wind*, and one can accordingly identify the disk surface z_s with the location where v_ϕ becomes equal to v_K . The mass outflow rate is fixed by the density at the sonic/sms point (marked by z_{sms} on the diagram).

The Hydrostatic Approximation

The structure equations of the radially localized disk model can be simplified by setting $v_z \approx 0$. Although this approximation is most appropriate for the quasi-hydrostatic region, one can nevertheless extend it to the disk surface to obtain useful algebraic constraints on viable disk solutions. For the pure ambipolar regime (and again assuming $\rho_i = \text{const}$), they are given by (Wardle & Königl 1993; Königl 1997)

$$(2\mathcal{Y}_0)^{-1/2} \lesssim a_0 \lesssim \sqrt{3} \lesssim \epsilon\mathcal{X}_0 \lesssim v_K/2C, \quad (84)$$

where the parameter \mathcal{Y}_0 represents the midplane Elsasser number in the ambipolar limit (see Eq. (25)). The four inequalities in Eq. (84) have the following physical meaning (going from left to right):

1. The disk remains sub-Keplerian everywhere below its surface.
2. The wind launching condition ($b_{r,s} > 1/\sqrt{3}$) is satisfied.
3. The top of the disk (z_s) exceeds a density scale height ($h \approx (a_0/\epsilon\mathcal{Y}_0)h_T$), ensuring that the bulk of the disk material is nearly hydrostatic and that \dot{M}_w remains $\ll \dot{M}_a$.³⁰
4. The midplane Joule heating rate (see Sect. 2.4) is less than the rate of gravitational potential energy release there ($\rho_0|v_{r,0}|v_K^2/2r$ per unit volume), as the latter is the ultimate source of energy production in the disk.

The inequalities (1) and (2) together place a lower bound on the neutral-field coupling parameter \mathcal{Y}_0 , for which a more detailed analysis yields the value of ~ 1 (see Königl et al. 2010). The inequalities (2) and (3), in turn, imply that $h/h_T < 1$, i.e., that magnetic squeezing dominates tidal gravity. Analogous constraints on wind-driving disks can be obtained also in the Hall and Ohm diffusivity regimes. For example, in the Hall case the parameter space divides into four sub-regimes with distinct sets of constraints (Königl et al. 2010; Salmeron et al. 2010). In all of these cases it is inferred that $\mathcal{Y}_0 > 1$ and $h/h_T < 1$, which indicates that these are generic properties of wind-driving disks. In practice one finds that successful full solutions typically have $a_0 \lesssim 1$ (the midplane magnetic pressure is smaller than the thermal pressure, but not greatly so) and $\epsilon \lesssim 1$ (the midplane inflow speed is not much smaller than the speed of sound).

³⁰ These requirements also place upper limits on the ratio of the density at the sonic/sms point to the midplane density (see Eq. (78) for the sms case).

The relations listed in Eq. (84) have a few other interesting implications. For example, one can use the inequality (3) to argue that wind-driving disks are stable to the fastest growing linear mode of the MRI, because it implies that the vertical wavelength of this mode, $\sim v_{A0}/\Omega_K$ (see Chap. V), is larger than the magnetically reduced disk scale height $h = (a_0/\epsilon\mathcal{X}_0)C/\Omega_K$. But one can also argue that the inequality (1) leads to a useful criterion for the onset of the MRI in the disk. Such a criterion is of interest since, as we already noted when the Elsasser number was introduced in Sect. 2.4, the minimum-coupling condition for the development of MRI turbulence in a diffusive disk (represented by a lower bound on Λ) is evidently similar to that inferred for driving a disk wind. The question then arises as to whether, in a disk that is threaded by a large-scale, ordered field, both vertical (wind-related) and radial (MRI-related) angular momentum transport can occur at the same radial location; this can alternatively be phrased as a question about the maximum magnetic field strength for the operation of the MRI. When the inequality (1) is violated, the surface layers become super-Keplerian, implying outward streaming motion that is unphysical in the context of a pure wind-driving disk. However, as elaborated in Salmeron et al. (2007), such motion could be associated with the two-channel MRI mode that underlies MRI-induced turbulence. If one regards the parameter combination $2\Upsilon a^2$ that figures in this inequality as a function of height in the disk rather than being evaluated at the midplane, one can infer from the fact that it scales as $B_z^2(\varrho_i/\varrho)$ that it generally increases with z . It is thus conceivable that the inequality (1) (generalized in this manner) is violated near the midplane but is satisfied closer to the disk surface. Salmeron et al. (2007) developed disk models in which both radial turbulent transport and vertical transport associated with the *mean* field take place in the region where the inequality (1) is violated but only vertical transport (with ultimate deposition of the removed angular momentum in a disk wind) occurs at greater heights. They concluded, however, that significant radial overlap between these two transport mechanisms is unlikely to occur in real disks.

Weakly Coupled Disks

In the disk models considered so far, the minimum-coupling condition on the neutrals, $\Lambda \gtrsim 1$, was satisfied throughout the vertical extent of the disk. We refer to such disks as being *strongly coupled*. As we have, however, just noted, the parameter values in a real disk could vary with height, reflecting the vertical stratification of the column density (which shields the ionizing radiation or cosmic rays) and the density. In particular, if the disk is in the ambipolar regime near the surface, in the Hall regime further down, and in the Ohm regime near the midplane, then Λ scales as ϱ_i , ϱ_i/ϱ , and ϱ_i/ϱ^2 , respectively, on going from $z = z_s$ to $z = 0$ (see Eq. (25)). The Elsasser number will thus increase with height on moving up from $z = 0$ as the gas becomes progressively more ionized and the density decreases. It will generally

peak on reaching the ambipolar regime and will subsequently drop as q_i (which typically scales as ϱ to a power between 0 and 0.5) decreases. The gas will be weakly coupled in regions where Λ remains $\ll 1$. Weakly coupled disks have distinct properties from those of strongly coupled ones, as first pointed out by Li (1996a).

As an example, consider a protostellar disk that is ionized solely by cosmic rays (with the ionization rate decreasing exponentially with depth into the disk with a characteristic attenuation column of 96 g cm^{-2}) and in which the charge carriers are small, singly charged grains of equal mass (a reasonable approximation for the high-density inner regions of a real disk; e.g., Neufeld & Hollenbach 1994). Near the disk surface the gas is in the ambipolar regime, but if the disk half-column is $\gg 96 \text{ g cm}^{-2}$, the degree of ionization near the midplane is very low and the gas there is in the Ohm regime.³¹ Figure 7, taken from Wardle (1997), depicts two illustrative solutions obtained for different radii in this model. The solution on the left corresponds to a large enough radius (and, correspondingly, a sufficiently low disk column) for the disk to be in the ambipolar regime throughout its vertical extent. By contrast, the solution on the right depicts a smaller radius where the column density is large and the disk is weakly ionized (and in the Ohm regime) near the midplane.

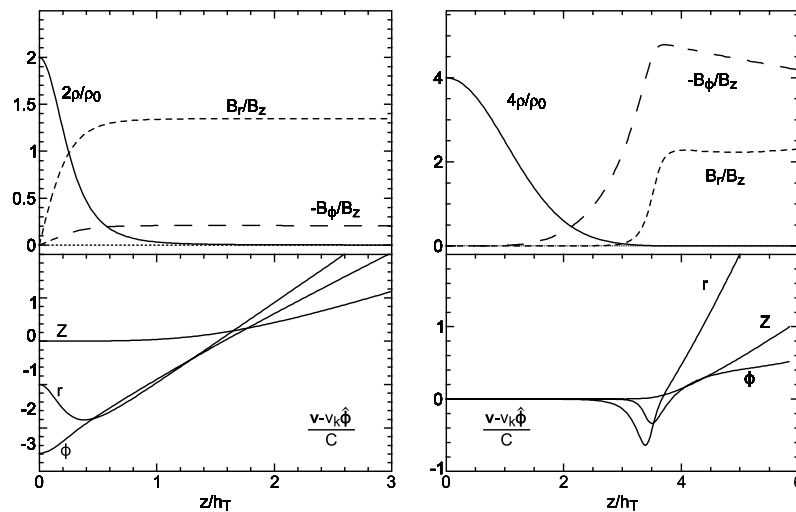


Fig. 7. Strongly coupled (left) vs. weakly coupled (right) disk solutions.

The main differences between these two solutions can be summarized as follows:

³¹ Owing to the assumed equal mass of the positive and negative charge carriers, the Hall term in Ohm's Law is identically zero (see Eq. (13)).

Strongly coupled disks

- $v_{A0} \lesssim C$ (midplane magnetic pressure comparable to thermal pressure);
- $|\langle v_r \rangle| \sim C$ (mean radial speed comparable to the speed of sound);
- $B_{r,s} > |B_{\phi,s}|$ (with B_r increasing already at $z = 0$).

Weakly coupled disks

- $v_{A0} \ll C$ (midplane magnetic field is highly subthermal);
- $|\langle V_r \rangle| \ll C$ (mean inflow speed is highly subsonic);³²
- $B_{r,s} < |B_{\phi,s}|$ (with B_r taking off only when Λ increases above ~ 1).³³

There are two noteworthy features of weakly coupled disk solutions. First, even though the bulk of the disk volume is nearly inert, the disk possesses “active” surface layers where $\Lambda > 1$, from which a disk wind can be launched in the presence of a large-scale, ordered field (or in which MRI-induced turbulence can operate; see Gammie 1996). Second, in magnetically threaded disks angular momentum is transported vertically even in regions where Λ is still < 1 and $B_r \approx 0$. This is because a measurable azimuthal field component can already exist in these regions ($|B_\phi/B_r|$ can be $\gg 1$ when $\Lambda \ll 1$; see footnote 33) and we recall that the $z\phi$ stress exerted by the field is $\propto B_z dB_\phi/dz$. As a result, matter can continue to accrete even in the nominally inert disk regions, which would not be possible if only a small-scale, disordered field (i.e., MHD turbulence) were responsible for angular momentum transport (although in practice turbulent mixing of charges and field might enable accretion in these regions also in that case; e.g., Fleming & Stone 2003; Turner et al. 2007). This could have implications to the ongoing debate about the nature of “dead zones” in protostellar disks (e.g., Pudritz et al. 2007; see Chap. V).

4.5 Stability Considerations

It was noted in Sect. 4.4 that wind-driving disks should be stable to the most rapidly growing linear mode of the MRI. On the other hand, by combining the

³² These solutions can thus evade the short-lifetime criticism made against strongly coupled disk models, namely, that in the absence of a vigorous mass supply (which only happens during the early evolutionary phases of protostars) they would empty out on a relatively short time scale (e.g., Shu et al. 2008). Recall in this connection that the disk formation models described in Sect. 3.4 yielded asymptotic ($r \rightarrow 0$) solutions that correspond to weakly coupled disks. The short-lifetime conundrum could be avoided altogether even in a strongly coupled disk if angular momentum transport by a wind only dominated in the innermost disk regions, which is not inconsistent with existing observational data.

³³ Using the hydrostatic approximation one can derive a differential equation relating B_r and B_ϕ , which, assuming $\epsilon_B = 0$ and a vanishing Hall term, takes the form $\frac{dB_r}{dB_\phi} \approx -2\Lambda$ at the midplane.

wind-launching condition (6) with the condition for the onset of a radial *interchange instability* (e.g., Spruit et al. 1995), one can show (see Königl & Wardle 1996) that, to be unstable to radial interchange, the magnetic term must be comparable to the gravitational term in the radial momentum equation. This is clearly not the case in the derived disk solutions, which are characterized by an inherently subthermal magnetic field (see, e.g., the inequality (2) in Eq. (84)). It is thus seen that, when a large-scale magnetic field is responsible for the entire angular momentum removal from an accretion disk through a CDW, it automatically lies in a “stability window” in which it is strong enough not to be affected by the MRI but not so strong as to be subject to radial interchange.

There are, of course, other potential instabilities to which such disks might be susceptible (see Königl & Wardle 1996 for some examples), but here we focus on the question of whether there might be an inherent aspect of the wind-related angular momentum transport that could render the disk/wind system unstable.³⁴ Based on approximate equilibrium models, Lubow et al. (1994b) and Cao & Spruit (2002) suggested that an inherent instability of this sort may, in fact, exist (see also Campbell 2009). They attributed this instability to the sensitivity of the outflowing mass flux to changes in the field-line inclination at the disk surface (θ_s), according to the following feedback loop:

$$\begin{aligned}
 |v_r| \text{ increases} &\Rightarrow \tan \theta_s \text{ increases} \\
 &\Rightarrow \text{the wind is loaded by higher-density gas} \\
 &\Rightarrow \dot{M}_w \text{ (and the removed angular momentum } \dot{M}_w l) \text{ increase} \\
 &\Rightarrow |v_r| \text{ increases even more....}
 \end{aligned}$$

The issue was reexamined by Königl (2004), who used the disk/wind model of Wardle & Königl (1993) and appealed to the fact that the stability properties generally change at a *turning point* of the equilibrium curve in the solution parameter space. Figure 8 depicts such equilibrium curves, labeled by their vertically constant Elsasser-number values $\Lambda = \Upsilon$, in the Blandford & Payne (1982) $\kappa - \lambda$ wind parameter space. The lower branches of these curves end on the long dashed curve, below which the outflows remain sub-Alfvénic, whereas the upper branches end on the short-dashed curve, to the right of which the surface layers of the disk are super-Keplerian. Any particular solution is determined by the value of the disk parameter $a_0 = (2/\gamma\beta_0)^{1/2}$, which increases along each $\Lambda = \text{const}$ curve from its minimum value on the “super-Keplerian” boundary (see the inequality (1) in Eq. (84)). It is seen that each

³⁴ A distinct, but still relevant, question is whether the wind by itself may be unstable. Numerical simulations that treated the disk as providing fixed boundary conditions for the outflow have indicated that the wind should not be disrupted, even in the presence of nonaxisymmetric perturbations (e.g., Anderson et al. 2006; Pudritz et al. 2007). However, these simulations did not account for the existence of a feedback between the wind and the disk.

curve exhibits a turning point.³⁵ This behavior can be understood as follows. The vertical hydrostatic equilibrium equation implies $b_{r,s}^2 \approx 2/a_0^2$ (assuming $B_{r,s}^2 \gg B_{\phi,s}^2$), and since $|B_\phi|$ evolves with B_r (see footnote 33), it follows that $|B_{\phi,s}|/B_z$, and hence the magnitude of the angular momentum that the outflow must carry away, increases with decreasing a_0 . Initially, as a_0 decreases from ~ 1 , $b_{r,s} = B_{r,s}/B_z$ increases rapidly, and the corresponding increase in the cylindrical radius of the Alfvén surface (the effective lever arm for the back torque exerted by the outflow on the disk, which scales as $\lambda^{1/2}$) increases the value of λ and leads to a reduction in the ratio of the mass outflow to the mass inflow rates (estimated as $\dot{M}_w/\dot{M}_a \approx 1/[4(\lambda - 1)]$). However, as a_0 continues to decrease, the rate of increase of $b_{r,s}$ declines while that of $|B_{\phi,s}|/B_z$ increases, and eventually the mass outflow rate must start to increase (with λ going down) to keep up with the angular momentum removal requirements. The transition between these two modes of enhanced angular momentum transport: predominantly by the lengthening of the lever arm (on the lower branch) vs. mainly by a higher mass-loss rate (on the upper branch) occurs at the turning point of the solution curve. One can determine which of the two solution branches is stable and which is not by considering the competition between radial advection and diffusion on the magnetic flux evolution (best done in the $a_0 - \lambda$ plane), in analogy with thermal stability arguments that analyze the relative magnitude of heating and cooling on each side of the thermal equilibrium curve. In this way one finds that the upper branch of the curves in Fig. 8 is unstable: this is the branch along which an increase in the angular momentum transport is accomplished through a higher mass outflow rate, precisely the behavior invoked in the heuristic instability argument reproduced above. Since, however, there is an alternative way of increasing the angular momentum transport (namely, through a lengthening of the effective lever arm), there is also a stable branch of the solution curve. Physically, the reason why a perturbation that reduces the field inclination to the disk does not necessarily trigger an instability is that an increase in $b_{r,s}$ also results in greater field-line tension, which tends to oppose the inward poloidal field bending. Whether a given solution branch is stable or not is determined by the extent to which this stabilizing effect can overcome the destabilizing influence of increased angular momentum removal brought about by the field-line bending.

It is possible to argue (see Königl 2004) that real protostellar systems likely correspond to the stable branches of the solution curves. Global numerical simulations could, however, shed more light on this question, as they have already started to do. For example, Casse & Keppens (2002) solved the nonideal MHD equations (assuming axisymmetry and a polytropic gas) and demonstrated jet launching by resistive disks. These results are significant on two main counts: first, they corroborate the basic picture of a magnet-

³⁵ This feature of the solution curves is also found in the corresponding plots in the $a_0 - \lambda$ plane, where now κ varies along each $A = \text{const}$ curve.

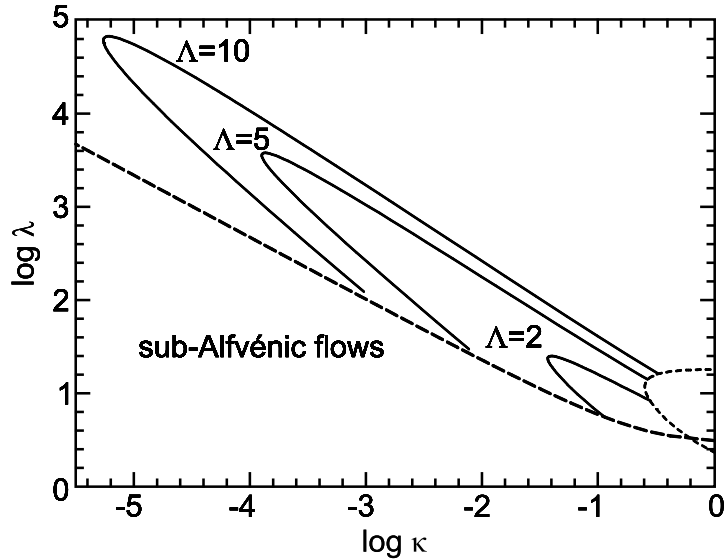


Fig. 8. Mapping of the wind-driving disk solutions (for several values of the neutral-field coupling parameter Λ) onto the self-similar wind solution space (defined by the values of the mass-loading parameter κ and angular-momentum parameter λ). The field-strength parameter a_0 increases on moving counterclockwise along a given curve.

ically threaded diffusive disk centrifugally driving a wind that removes the bulk of its angular momentum, and, second, they indicate that these configurations are stable inasmuch as they reach a quasi-steady state. Subsequent simulations have extended this work while confirming its main conclusions (e.g., Kuwabara et al. 2005; Meliani et al. 2006; Zanni et al. 2007). Three-dimensional simulations are the natural next step.

5 Disk–Star Magnetic Coupling

We now turn to the best-established example of a large-scale field in protostars, namely, the stellar dynamo-generated field, and consider the dynamical interaction between this field and the surrounding accretion disk. This is a rich topic that has implications to the structure of the innermost disk region, the stellar rotation and the way mass reaches the stellar surface, protostellar jets, and the observational signatures of the region where most of the gravitational potential energy is liberated. Owing to the nontrivial topology of the stellar (and possibly also disk-generated) magnetic field and to the complexity of the field-mediated interaction between the star and the disk even for

simple flux distributions, our understanding is far from complete, with new progress being driven largely by improved numerical simulations. We start this section by briefly surveying the relevant observations and then describe the basic physical processes that underlie this interaction and the results of some of the recent numerical work. Relevant additional details are provided in Chap. I [Protoplanetary Disk Structure and Evolution].

5.1 Phenomenology

We discuss the observational manifestations of two phenomena in which a large-scale, ordered magnetic field has been implicated: the relationship between protostellar rotation and accretion disks, and magnetic disk truncation and resultant field-channeled accretion. The theoretical framework that relates these two phenomena is outlined in the next subsection.

Stellar Rotation and Accretion

It is now well established (based on ~ 1700 measured rotation periods) that about 50% of sun-like protostars ($M_* \sim 0.4 - 1.2 M_\odot$) undergo significant rotational braking during their pre-main-sequence (PMS) contraction to the Zero-Age Main Sequence (ZAMS), and that the objects whose specific angular momenta decrease with time are essentially the ones that are already slowly rotating at an early (~ 1 Myr) age (e.g., Herbst et al. 2007). A clue to the braking mechanism is provided by the finding of a clear correlation between having a comparatively long period ($\gtrsim 2$ d) and exhibiting an accretion-disk signature (near-IR or mid-IR excess). This trend is particularly noticeable in higher-mass ($\gtrsim 0.25 M_\odot$) protostars, but it is also found in very-low-mass stars and brown dwarfs (in which, however, the braking efficiency is evidently lower). The connection with disks is supported by the fact that the inferred maximum stellar braking times ($\sim 5 - 10$ Myr) are comparable to the maximum apparent lifetimes of gaseous accretion disks (which are ~ 1 Myr for $\sim 50\%$ of the stars and ~ 5 Myr for almost all stars). These results imply that the dominant braking mechanism in protostars is directly tied to active disk accretion. In the absence of such accretion (or after the disks disperse), PMS stars nearly conserve specific angular momentum and therefore spin up as they contract to the ZAMS. As we discuss in the next subsection, stellar magnetic fields likely play a key role in the braking process.

Disk Truncation and Field-Channeled Accretion

As was originally inferred in the case of accreting magnetized neutron stars and white dwarfs, a sufficiently strong protostellar magnetic field can be expected to *truncate the accretion flow*, with the truncation radius increasing with B_* and decreasing with \dot{M}_a (see Eqs. (85) and (86) below). In this picture, the intercepted matter “climbs” onto the field lines and is *magnetically channeled* to some finite stellar latitude. By the time the matter reaches the

stellar surface it is streaming along the field lines with a near free-fall speed and is therefore stopped in an *accretion shock*. The basic elements of this scenario are supported by observations of CTTSs (but also of lower-mass brown dwarfs and of higher-mass Herbig Ae/Be stars, although so far these have been less well-studied). The main findings have been (see Bouvier et al. 2007):

- The common occurrence of inverse P Cygni profiles, with redshifted absorption reaching several hundred km s^{-1} .
- Observed hydrogen and Na I line profiles that can be adequately modeled in this picture; the detection in the UV–near-IR spectral range of predicted statistical correlations between the line fluxes and the inferred mass accretion rate.
- Observed spectral energy distributions of optical and UV excesses that are successfully reproduced by accretion shock models.
- Periodic visual-flux variations due to “hot spots” (interpreted as non-axisymmetric accretion shocks on the stellar surface) that are only observed in actively accreting CTTSs (but *not* in the weak-line T Tauri stars (WTTSs), which lack the signatures of vigorous accretion). However, in contrast to “cool spots” (the analogs of sunspots), which last for $\sim 10^2 - 10^3$ rotations, the hot-spot periodicity only persists for a few rotation periods, indicating a highly nonsteady configuration. This inference is supported by the detection of high-amplitude irregular flux variations.
- Strong near-IR “veiling” variability that can be interpreted in the context of this picture as arising in the interaction region between the disk and an inclined stellar magnetosphere, with possible contributions also from the accretion shock and from the shock-irradiated zone in the inner disk.

Zeeman-broadening measurements in a growing number of CTTSs have yielded an intensity-averaged mean surface magnetic field strength of $\sim 2.5 \text{ kG}$,³⁶ with the field inferred to reach $\sim 4 - 6 \text{ kG}$ in some regions. Furthermore, circular polarization measurements in lines associated predominantly with the accretion shock have revealed rotational modulation and demonstrated that the field is highly organized (with peak value $\sim 2.5 \text{ kG}$) in the shock region (covering $< 5\%$ of the stellar surface). These results are consistent with the model predictions. No net polarization has, however, been found in photospheric absorption lines, implying a complicated surface field topology (with a global dipole component $\lesssim 0.1 \text{ kG}$). A likely physical picture is that there exists a spectrum of magnetic flux loops of various lengths that extend from the stellar surface, with a fraction reaching to $\sim 5 - 20 R_*$ and intercepting the disk (see Feigelson et al. 2007). This picture is supported by analyses of X-ray flares from young stars (e.g., Favata et al. 2005) as well as by direct radio imaging of the large-scale magnetic structures (e.g., Loinard

³⁶ A similar value has now been inferred also in a protostar that is at an earlier (Class I) evolutionary phase (Johns-Krull et al. 2009).

et al. 2005) and by spectropolarimetric reconstructions of the magnetospheric topology (e.g., Donati et al. 2007).

Numerical studies of magnetospheric accretion indicate that disk mass-loaded *outflows* (which are often predicted to be nonsteady) could be produced in the course of the star–disk interaction (see Sect. 5.2). There is now observational evidence for accretion-induced winds in CTTSs emanating from both the inner disk and the star (e.g., Edwards et al. 2006). The stellar component has been inferred to move on radial trajectories and to undergo full acceleration (up to a few hundred km s^{-1}) in the stellar vicinity. Although this component may well be launched along stellar magnetic field lines, the absence of evidence for it in WTTSs suggests that it, too, is triggered by the interaction with the disk.

5.2 Disk–Star Coupling Models

Basic Concepts

Spherical accretion with $\dot{M}_a = 4\pi R^2 \rho(R) |V_R(R)|$ at the free-fall speed $v_{\text{ff}}(R) = (2GM_*/R)^{1/2}$ onto a star of mass M_* will be stopped by the magnetic stresses of the stellar magnetic field at a distance where the ram pressure of the flow (ρv_{ff}^2) becomes comparable to the magnetic pressure of the stellar field ($B^2/8\pi$). For simplicity, we assume that the field at that location can be approximated by its dipolar component (corresponding to a dipole moment μ_*). For accretion in the equatorial plane, $B(r) = \mu_*/r^3 = B_* R_*^3/r^3$, and one obtains the nominal *accretion Alfvén radius*

$$r_A = \frac{\mu_*^{4/7}}{(2GM_*)^{1/7} \dot{M}_a^{2/7}}. \quad (85)$$

Although the radial ram pressure of the flow is relatively small for disk accretion, one can still define in this case a magnetospheric boundary radius r_m from the requirement that the total material and magnetic stresses (or energy densities) be comparable, i.e., $B^2/8\pi = \rho v_\phi^2 + P \approx \rho v_\phi^2$. By approximating $v_\phi \approx v_K$, one obtains an expression similar to the one given by Eq. (85). This radius determines the region within which the stellar magnetic field controls the flow dynamics and provides a lower bound on the inner disk radius. To estimate the radius where matter leaves the disk, note that the physical process of disk truncation requires that the torque exerted by the stellar field that penetrates the disk be comparable to the rate at which angular momentum is transported inward by the accretion flow, $-r^2 B_z B_{\phi,s} = \dot{M}_a d(r^2 \Omega)/dr$. Taking $|B_{\phi,s}| \approx B_z$ (where we use the approximate maximum value of the azimuthal field component at the disk surface; see Uzdensky et al. 2002a and cf. Eq. (38)) and setting $|d\Omega/dr| \sim \Omega_K/r$ yields an estimate of the *disk truncation radius* r_d that is of the order of r_A ,

$$r_d = k_A r_A. \quad (86)$$

Semianalytic models (e.g., Ghosh & Lamb 1979) and numerical simulations (e.g., Long et al. 2005) yield $k_A \approx 0.5$.

If the star is rotating with angular velocity Ω_* , one can define the *corotation radius* by setting $\Omega_K(r) = \Omega_*$, which gives

$$r_{\text{co}} = \left(\frac{GM_*}{\Omega_*^2} \right)^{1/3}. \quad (87)$$

The interaction of the disk with the stellar magnetic field naturally divides into two qualitatively different regimes depending on the ratio r_d/r_{co} :

$$\begin{array}{ll} r_d \lesssim r_{\text{co}} & \text{funnel-flow regime} \\ r_d \gtrsim r_{\text{co}} & \text{propeller regime.} \end{array}$$

In the funnel-flow regime, the disk angular velocity is higher than that of the star, and matter can climb onto the stellar magnetic field lines that thread the disk and reach the stellar surface. By contrast, in the propeller regime the stellar angular velocity exceeds $\Omega_K(r_d)$: when disk matter becomes attached to the stellar field lines its angular momentum increases above the rotational equilibrium value for that radius and it moves outward. Numerical simulations have found that, if the disk effective viscosity and magnetic diffusivity are relatively high, most of the incoming matter is expelled from the system, both in the form of a wide-angle CDW from the inner regions of the disk and as a strong, collimated, magnetically dominated outflow along the open stellar field lines near the axis (e.g., Romanova et al. 2005; Ustyugova et al. 2006).³⁷ This mechanism could be relevant to the initial spindown (on a time scale $< 10^6$ yr) of CTTSs.

Funnel-Flow Regime

Ghosh & Lamb (1979) proposed that a “disk locked” state in which the torque exerted by the field lines that thread the disk (as well as by the material that reaches the star) could keep the star rotating in equilibrium (neither spinning up nor down). In this picture, the field lines that connect to the disk within the corotation radius (as well as the accreted material) tend to spin the star up, whereas the field lines that connect at $r > r_{\text{co}}$ have the opposite effect. This scenario could potentially explain the relatively low rotation rates observed in CTTSs (e.g., Königl 1991).³⁸

This picture was, however, challenged on the grounds that the twisting of the magnetic field lines that thread the disk at $r > r_{\text{co}}$ will tend to open

³⁷ A similar outflow pattern, comprising a conical disk wind and a higher-velocity, low-density jet component, was found also in simulations of the funnel-flow regime (e.g., Romanova et al. 2009).

³⁸ Naively, one would expect a star accreting from a rotationally supported disk to rotate near breakup speed; in reality, CTTSs rotate, on average, at about a tenth of this speed.

them up, thereby reducing the spin-down torque on the star by more than an order of magnitude compared to the original calculation (Matt & Pudritz 2004, 2005). This argument is based on the fact that stellar field lines that connect to the disk at $r \neq r_{\text{co}}$ are twisted by the differential rotation between their respective footpoints. Initially, the twisting leads to an increase in $|B_{\phi,s}|$, but then the built-up magnetic stress causes the field lines to rapidly elongate in a direction making an angle $\sim 60^\circ$ to the rotation axis (e.g., Lynden-Bell & Boily 1994). During this phase $|B_{\phi,s}|$ decreases as the field-line twist travels out to the apex of the elongating field line, where the field is weakest, a process that can be understood in terms of torque balance along the field line (e.g., Parker 1979). As the twist angle approaches a certain critical value (~ 4 rad for a star linked to a Keplerian disk), the expansion accelerates and the magnetic field formally reaches a singular state (a “finite time singularity”), which in practice means that it opens up. While the twisting can be countered by magnetic diffusivity in the disk, this is only possible if the steady-state surface azimuthal field amplitude $(2\pi r \mathcal{S} \Delta\Omega / c^2) B_{z,s}$, where \mathcal{S} is the vertically integrated electrical conductivity (treated as a scalar) and $\Delta\Omega$ is the differential rotation rate, does not exceed the maximum value of $|B_{\phi,s}|$ in the absence of diffusivity (e.g., Uzdensky et al. 2002a). The conductivity in the innermost regions of protostellar disks is probably too high for a steady state to be feasible except in the immediate vicinity of r_{co} (see also Zweibel et al. 2006), and in some proposed models (e.g., the X-wind; see Shu et al. 2000) it has, in fact, been postulated that the stellar field lines can effectively couple to the disk only in that narrow region.

Numerical simulations have, however, verified that, when the star has a strong enough field to disrupt the disk at a distance of a few stellar radii and channel accreting matter along field lines, it can maintain an equilibrium disk-locking state in which Ω_* is close to the disk angular velocity at the truncation radius (Long et al. 2005). In these simulations it was found that, in equilibrium, $r_{\text{co}}/r_{\text{d}} \sim 1.2 - 1.5$, very close to the prediction of the Ghosh & Lamb (1979) model. Furthermore, as envisioned in the latter model, closed magnetic field lines that link the star and the disk exert the dominant stresses in this interaction. However, in contrast to the original picture, this linkage does in fact occur primarily near r_{co} . The torque balance is achieved in part through field-line stretching (which mimics the connection to material at $r > r_{\text{co}}$ in the original model) and by magnetically driven outflows (which, however, are found to remain comparatively weak in the simulations). Field-line opening is not a major impediment to this process, in part because opened field lines tend to reconnect (especially if the departure from axisymmetry is not large).³⁹

³⁹ The idea that twisted field lines that open up could subsequently reconnect, leading to a repetitive cycle of inflation and reconnection and resulting in the star-disk linkage being steady only in a time-averaged sense, was first proposed by Aly & Kijpers (1990) and received support from subsequent investigations (e.g., Uzdensky et al. 2002b; Romanova et al. 2002).

The question of whether (or under what circumstances) the magnetic transfer of angular momentum to the disk is the most efficient way of attaining protostellar spin equilibrium is, however, still unresolved. For example, Matt & Pudritz (2008) suggested that stellar winds driven along open magnetic field lines could dominate the braking torque on the star. These winds are inferred to be powered by the accretion process, but it remains to be determined how this could happen in practice and whether the proposed outflows are, in fact, related to the stellar winds already identified observationally. It is also important to bear in mind that the star–disk magnetic linkage mechanism may, in reality, be more complex than the simplified picture outlined above. Some of these expected complications are already being investigated with the help of 3D MHD codes, including the effects of misalignment between the rotation and magnetic axes, of an off-centered dipole, and of higher-order multipole moments (e.g., Romanova et al. 2003, 2004, 2008; Long et al. 2007, 2008; Kulkarni & Romanova 2009).⁴⁰ Furthermore, the field topology and the nature of the interaction could be modified if the disk itself contains a large-scale magnetic field (e.g., Hirose et al. 1997; Miller & Stone 2000; Ferreira et al. 2000, 2006; von Rekowski & Brandenburg 2004, 2006).

Nonsteady accretion

The magnetic interaction between stars and disks could be variable on a time scale as short as Ω_*^{-1} . One possibility, which could naturally give rise to observable “hot spots,” is for the system to lack axisymmetry — either because of a misalignment between the magnetic (e.g., dipole) and rotation axes (e.g., Romanova et al. 2004, 2008; Kulkarni & Romanova 2009) or because of the intrinsic structure of the magnetic field (e.g., von Rekowski & Brandenburg 2004, 2006). A longer variability time scale is implied by the suggestion of Goodson & Winglee (1999) that the truncation radius would oscillate on the diffusion time scale of the field into the disk (resulting in field-line reconnection events and episodic polar ejections) if the diffusivity at the inner edge of the disk were relatively low (so $|(v_{B,r}/v_r) - 1| < 1$). A different type of variability is implied by the star/disk dynamo model of von Rekowski & Brandenburg (2006). In this model, the magnetic field geometry changes at irregular time intervals (with magnetic polarity reversals occurring mostly on time scales of less than a day), and the star/disk system alternates between magnetically connected and disconnected states. The model predicts strong outflows, both from the inner disk and from the stellar surface, but typically only a small fraction of the disk accretion flow reaches the stellar surface. In fact, there is an anti-correlation between the stellar magnetic field strength and the accretion rate, and material that reaches the stellar surface comes in at a low velocity

⁴⁰ Given the importance of the question of how matter crosses magnetic field lines in this problem, it would be helpful to examine these effects using an explicitly resistive numerical code. So far, however, only the axisymmetric version of this scenario has been investigated in this way (e.g., Bessolaz et al. 2008).

(von Rekowski & Piskunov 2006). It remains to be determined whether these two aspects of the model are consistent with the polarization data and the evidence for accretion shocks (see Sect. 5.1).

6 Conclusion

The discussion in this chapter can be summarized as follows:

- There is strong observational evidence for a disk–wind connection in protostars. Large-scale, ordered magnetic fields have been implicated theoretically as the most likely driving mechanism of the observed winds and jets. The ubiquity of the outflows may be related to the fact that centrifugally driven winds (CDWs) are a potentially efficient means of transporting angular momentum from the disk.
- Ordered magnetic fields could arise in protostellar disks on account of (*i*) advection of interstellar field by the accretion flow, (*ii*) dynamo action in the disk, and (*iii*) interaction with the stellar magnetic field.
- Semianalytic MHD models have been able to account for the basic structure of diffusive disks that drive CDWs from their surfaces as well as for the formation of such systems in the collapse of rotating molecular cloud cores. Some of these models already incorporate a realistic disk ionization and conductivity structure. These studies have established that vertical angular momentum transport by a CDW or through torsional Alfvén waves (magnetic braking) could in principle be the main angular momentum removal mechanism in protostellar disks and determined the parameter regime where wind transport can be expected to dominate radial transport by MRI-induced turbulence. Further progress is being made by increasingly more elaborate numerical simulations (involving nonideal MHD codes) that have started to examine the global properties, time evolution, and dynamical stability of the magnetic disk/wind system.
- Robust observational evidence also exists for a magnetic interaction between CTTS disks and their respective protostars, including strong indications of a field-channeled flow onto the stellar surface. This interaction is likely to involve mass ejection and is thought to be responsible for the comparatively low rotation rates of CTTSs. Since the magnetic field geometry in the interaction region is evidently quite complex and the interaction is likely time dependent, numerical simulations are an indispensable tool in the study of this problem.

Future advances in this area will probably arise from a combination of new observational findings, the refinement of current theoretical approaches, and the incorporation of additional physics into the models. On the observational side, the main challenge is still to demonstrate the existence of CDWs in protostars and to determine their spatial extent (spread out over most of the disk surface or occurring only near its inner edge, and, if the former, is the

launching region nearly continuous or is it confined to localized patches?). Recent attempts to measure rotation in the outflows could potentially help to answer this question, but, as noted in Sect. 2.3, the results obtained so far are still inconclusive.

Regarding the further development of theoretical tools, the greatest impact would likely be produced by numerical simulations that study vertical angular momentum transport by either a CDW or magnetic braking with codes that include a realistic conductivity tensor and that have full 3D and mesh-refinement capabilities. Such simulations should be able to clarify the relative roles of vertical and radial angular momentum transport and the possible interplay between them for relevant combinations of the disk model parameters (see Sect. 4.4). An interim step might be to solve for the evolution of a vertically integrated disk whose properties, at any radial grid zone, are determined from a vertical integration of a simplified version of the radially localized, steady-state disk model described in Sect. 4.4. Time-dependent models of this type could examine the behavior of a magnetically threaded disk after its mass supply diminishes or stops altogether (corresponding to the protostellar system evolving into the optically revealed phase), which has previously been studied only in the context of “ α -viscosity” models. As was already noted above, a state-of-the-art, 3D, nonideal-MHD code is also crucial for investigating the stability of disk/wind systems and the various aspects of the star–disk field-mediated interaction. One could, however, also benefit from further development of the semianalytic models, which could include an extension of the ionization/conductivity scheme, a derivation of self-similar disk/wind solutions that allow for a radial drift of the poloidal magnetic field (see Sect. 4.4), and a calculation of the predicted observational characteristics of wind-driving disks.

The mass fraction and size distribution of dust grains in the disk have a strong effect on its ionization and conductivity structure and on the degree of field–matter coupling (see Sect. 4.4). Existing models incorporate the effect of dust in a somewhat ad-hoc manner, by adopting an assumed distribution. In reality, the grain distribution is determined by the balance of several processes, including grain collisions due to relative velocities that develop as a result of Brownian motion, differential vertical-settling speeds, and turbulence, which can lead to either coagulation or fragmentation. Grains are also subject to a collisional drag force exerted by the gas and arising from the fact that the gas is subject to thermal and magnetic forces that do not affect the dust. This leads to vertical settling as well as to radial migration, directed either inward or outward depending on whether the gas rotation is sub- or super-Keplerian, respectively. Furthermore, radial or vertical gas motions can affect sufficiently small grains through advection. Yet another effect is evaporation by the ambient radiation field, which could impact dust located at sufficiently high elevations and small radii. Some of these effects have already been incorporated into generic viscous disk models (e.g., Dominik et al. 2007; Brauer et al. 2008), and one could similarly consider them in the context of a

wind-driving disk model. In view of the fact that the latter model is characterized by a vertical outflow and by comparatively fast radial inflow speeds, one can expect to find new types of behavior in this case. In particular, grains located near the disk surfaces would either settle to the midplane if they are large enough or be uplifted from the disk if they are sufficiently small, whereas intermediate-size grains would first leave the disk and then re-enter at a potentially much larger radius, from which they could be advected back inward. By including dust dynamics, one could examine whether the effect of dust on the gas motion (through its influence on the field–matter coupling) and the effect of gas on the grain motions (through gas–dust collisions) together place meaningful constraints on the resulting grain distribution. One could also investigate whether the predicted radial transport of intermediate-size grains from small to large radii and their possible thermal processing outside the disk could be relevant to the accumulating evidence for an outward transport of crystalline grains in the protosolar nebula and in other protostellar disks, and whether the implied dust distribution in the disk and the wind might have distinct observational signatures that could be tested by spectral and imaging techniques (see Millan-Gabet et al. 2007, Sect. 4.3, and Chaps. I and VIII).

Dust particles are thought to be the building blocks of planetesimals and their distribution in the disk is thus a key ingredient of planet formation models. In fact, the general properties of a protostellar disk are evidently relevant to planet formation in light of the growing evidence that the latter is strongly influenced by physical processes that occur when the disk is still predominantly gaseous. A disk threaded by a large-scale, ordered magnetic field could potentially have unique effects on planet growth and migration. One such effect is the generation (through magnetic resonances that are the analogs of Lindblad resonances) of a global torque that may reduce, or even reverse, the secular inward drift (the so-called Type I migration) predicted for low-mass planets, which has posed a conundrum for current theories of planet formation. As was demonstrated by Terquem (2003) and Fromang et al. (2005), a torque of this type could be produced if the disk had a comparatively strong (MRI-stable, but still subthermal) azimuthal field (with a nonzero vertical average of B_ϕ^2) that fell off sufficiently fast with radius ($\propto r^{-1} - r^{-2}$). A poloidal field component could in principle also contribute to this process (Muto et al. 2008). Given that a large-scale field with precisely these properties is expected in wind-driving protostellar disks (see Sects. 3 and 4), this possibility clearly merits an explicit investigation in the context of the disk models considered in this chapter. The influence of the vertical channel of angular momentum transport and of the overall effect of an ordered, large-scale field on the disk structure in such systems (e.g., the reduction of the density scale height by magnetic squeezing) may also be worth examining in this connection.

Acknowledgments

The authors have greatly benefited from their collaborations over the years with Glenn Ciolek, Ioannis Contopoulos, Ruben Krasnopolsky, Christof Litwin, Pedro Safer, Konstantinos Tassis, Seth Teitler, Dmitri Uzdensky, Nektarios Vlahakis, and, in particular, Mark Wardle on the topics discussed in this chapter. They are also grateful to Marina Romanova for helpful correspondence on disk–star magnetic coupling. Their work was supported in part by NSF grant AST-0908184 (AK) and Australian Research Council grant DP0342844 (RS).

References

1. J. J. Aly, J. Kuijpers: *A&A* **227**, 473 (1990)
2. J. M. Anderson, Z.-Y. Li, R. Krasnopolsky, R. D. Blandford: *ApJ* **590**, L107 (2003)
3. J. M. Anderson, Z.-Y. Li, R. Krasnopolsky, R. D. Blandford: *ApJ* **653**, L33 (2006)
4. H. G. Arce, D. Shepherd, F. Gueth, C.-F. Lee, R. Bachiller, A. Rosen, H. Beuther: *Molecular Outflows in Low- and High-Mass Star-forming Regions*. In: *Protostars and Planets V*, ed by B. Reipurth, D. Jewitt, and K. Keil (Univ. of Arizona, Tucson 2007) p. 245
5. S. A. Balbus, J. C. B. Papaloizou: *ApJ* **521**, 650 (1999)
6. S. A. Balbus, C. Terquem: *ApJ* **552**, 235 (2001)
7. J. Bally, B. Reipurth, C. J. Davis: *Observations of Jets and Outflows from Young Stars*. In: *Protostars and Planets V*, ed by B. Reipurth, D. Jewitt, and K. Keil (Univ. of Arizona, Tucson 2007) p. 215
8. A. Balogh, E. J. Smith, B. T. Tsurutani, D. J. Southwood, R. J. Forsyth, T.S. Horbury: *Science* **268**, 1007 (1995)
9. S. Basu, T. Ch. Mouschovias: *ApJ* **432**, 720 (1994)
10. A. Belloche, P. André, D. Despois, S. Blinder: *A&A* **393**, 927 (2002)
11. N. Bessolaz, C. Zanni, J. Ferreira, R. Keppens, J. Bouvier: *A&A* **478**, 155 (2008)
12. E. G. Blackman, J. C. Tan: *Ap&SS* **292**, 395 (2004)
13. O. M. Blaes, S. A. Balbus: *ApJ* **421**, 163 (1994)
14. R. D. Blandford, D. G. Payne: *MNRAS* **199**, 883 (1982)
15. S. V. Bogovalov: *A&A* **323**, 634 (1997)
16. J. Bouvier, S. H. P. Alencar, T. J. Harries, C. M. Johns-Krull, M. M. Romanova: *Magnetospheric Accretion in Classical T Tauri Stars*. In: *Protostars and Planets V*, ed by B. Reipurth, D. Jewitt, and K. Keil (Univ. of Arizona, Tucson 2007) p. 479
17. A. Brandenburg, Å. Nordlund, R. F. Stein, U. Torkelsson: *ApJ* **446**, 741 (1995)
18. F. Brauer, C. P. Dullemond, Th. Henning: *A&A* **480**, 859 (2008)
19. S. Cabrit: *LNP* **723**, 21 (2007)
20. S. Cabrit, J. Ferreira, A. C. Raga: *A&A* **343**, L61 (1999)
21. S. Cabrit, J. Pety, N. Pesenti, C. Dougados: *A&A* **452**, 897 (2006)
22. N. Calvet, L. Hartmann, S. E. Strom: *Evolution of Disk Accretion*. In: *Protostars and Planets IV*, ed by V. Mannings, A. P. Boss, S. S. Russell (Univ. of Arizona, Tucson 2000) p. 377

23. C. G. Campbell: MNRAS **336**, 999 (2002)
24. C. G. Campbell: MNRAS **392**, 271 (2009)
25. X. Cao, H. C. Spruit: A&A **287**, 80 (1994)
26. X. Cao, H. C. Spruit: A&A **385**, 289 (2002)
27. F. Casse, R. Keppens: ApJ **581**, 988 (2002)
28. A. H. Cerqueira, P. F. Velázquez, A. C. Raga, M. J. Vasconcelos, F. de Colle: A&A **448**, 231 (2006)
29. A. Chrysostomou, F. Bacciotti, B. Nisini, T. P. Ray, J. Eisloffel, C. J. Davis, M. Takami: A&A **482**, 575 (2008)
30. A. Chrysostomou, P. W. Lucas, J. H. Hough: Nature **450**, 71 (2007)
31. G. E. Ciolek, A. Königl: ApJ **504**, 257 (1998)
32. G. E. Ciolek, T. Ch. Mouschovias: ApJ **418**, 774 (1993)
33. D. Coffey, F. Bacciotti, T. P. Ray, J. Eisloffel, J. Woitas: ApJ **663**, 350 (2007)
34. I. Contopoulos, G. E. Ciolek, A. Königl: ApJ **504**, 247 (1998)
35. I. Contopoulos, R. V. E. Lovelace: ApJ **429**, 139 (1994)
36. T. G. Cowling: *Magnetohydrodynamics*, (Adam Hilger, Bristol 1976)
37. R. M. Crutcher: ApJ **520**, 706 (1999)
38. J. Di Francesco, N. J. Evans II, P. Caselli, P. C. Myers, Y. Shirley, Y. Aikawa, M. Tafalla: An Observational Perspective of Low-Mass Dense Cores I: Internal Physical and Chemical Properties. In: *Protostars and Planets V*, ed by B. Reipurth, D. Jewitt, and K. Keil (Univ. of Arizona, Tucson 2007) p. 17
39. C. Dominik, J. Blum, J. N. Cuzzi, G. Wurm: Growth of Dust as the Initial Step toward Planet Formation. In: *Protostars and Planets V*, ed by B. Reipurth, D. Jewitt, and K. Keil (Univ. of Arizona, Tucson 2007) p. 783
40. J.-F. Donati, F. Paletou, J. Bouvier, J. Ferreira: Nature **438**, 466 (2005)
41. J.-F. Donati, et al.: MNRAS **380**, 1297 (2007)
42. C. Dougados, S. Cabrit, J. Ferreira, N. Pesenti, P. Garcia, D. O'Brien: Ap&SS **293**, 45 (2004)
43. B. T. Draine, W. G. Roberge, A. Dalgarno: ApJ **264**, 485 (1983)
44. J. E. Drew, D. Proga, J. M. Stone: MNRAS **296**, L6 (1998)
45. D. F. Duffin, P. R. Pudritz: ApJ **706**, L46 (2009)
46. J. A. Dutrey, S. Guilloteau, P. Ho: Interferometric Spectroimaging of Molecular Gas in Protoplanetary Disks. In: *Protostars and Planets V*, ed by B. Reipurth, D. Jewitt, and K. Keil (Univ. of Arizona, Tucson 2007) p. 495
47. S. Edwards, W. Fischer, L. Hillenbrand, J. Kwan: ApJ **646**, 319 (2006)
48. B. G. Elmegreen: ApJ **530**, 277 (2000)
49. B. G. Elmegreen: ApJ **668**, 1064 (2007)
50. F. Favata, E. Flaccomio, F. Reale, G. Micela, S. Sciortino, H. Shang, K. G. Stassun, E. D. Feigelson: ApJS **160**, 469 (2005)
51. E. Feigelson, L. Townsley, M. Güdel, K. Stassun: X-Ray Properties of Young Stars and Stellar Clusters. In: *Protostars and Planets V*, ed by B. Reipurth, D. Jewitt, and K. Keil (Univ. of Arizona, Tucson 2007) p. 313
52. J. Ferreira: A&A **319**, 340 (1997)
53. J. Ferreira, F. Casse: ApJ **601**, L139 (2004)
54. J. Ferreira, C. Dougados, S. Cabrit: A&A **453**, 785 (2006)
55. J. Ferreira, G. Pelletier: A&A **295**, 807 (1995)
56. J. Ferreira, G. Pelletier, S. Appl: MNRAS **312**, 387 (2000)
57. R. A. Fiedler, T. Ch. Mouschovias: ApJ **415**, 680 (1993)
58. T. Fleming, J. M. Stone: ApJ **585**, 908 (2003)

59. J. Frank, A. King, D. Raine: *Accretion Power in Astrophysics* (Cambridge University Press, Cambridge 2002).
60. S. Fromang, C. Terquem, S. A. Balbus: MNRAS **329**, 18 (2002)
61. S. Fromang, C. Terquem, R. P. Nelson: MNRAS **363**, 943 (2005)
62. D. Galli, F. H. Shu: ApJ **417**, 243 (1993)
63. C. F. Gammie: ApJ **457**, 355 (1996)
64. P. J. V. Garcia, J. Ferreira, S. Cabrit, L. Binette: A&A **377**, 589 (2001a)
65. P. J. V. Garcia, S. Cabrit, J. Ferreira, L. Binette: A&A **377**, 609 (2001b)
66. P. Ghosh, F. K. Lamb: ApJ **232**, 259 (1979)
67. J. M. Girart, R. Rao, D. P. Marrone: Science **313**, 812 (2006)
68. A. E. Glassgold, E. D. Feigelson, T. Montmerle: Effects of Energetic Radiation in Young Stellar Objects. In: *Protostars and Planets IV*, ed by V. Mannings, A. P. Boss, S. S. Russell (Univ. of Arizona, Tucson 2000) p. 429
69. A. E. Glassgold, E. D. Feigelson, T. Montmerle, S. Wolk: ASPC **341**, 165 (2005)
70. A. A. Goodman, P. J. Benson, G. A. Fuller, P. C. Myers: ApJ **406**, 528 (1993)
71. A. P. Goodson, R. M. Winglee: ApJ **524**, 159 (1999)
72. X. Guan, C. F. Gammie: ApJ **697**, 1901 (2009)
73. D. E. Harker, S. J. Desch: ApJ **565**, L109 (2002)
74. P. Hartigan, S. Edwards, L. Ghandour: ApJ **452**, 736 (1995)
75. L. Hartmann: The Observational Evidence for Accretion. In: *Herbig-Haro Flows and the Birth of Stars*, ed by B. Reipurth and C. Bertout (Kluwer, Dordrecht 1997) p. 391
76. L. Hartmann, S. J. Kenyon: ARA&A **34**, 207 (1996)
77. J. F. Hawley, J. M. Stone: ApJ **501**, 758 (1998)
78. P. Hennebelle, A. Ciardi: A&A **506**, L29 (2009)
79. R. N. Henriksen, D. R. Rayburn: MNRAS **152**, 323 (1971)
80. W. Herbst, J. Eislöffel, R. Mundt, A. Scholz: The Rotation of Young Low-Mass Stars and Brown Dwarfs. In: *Protostars and Planets V*, ed by B. Reipurth, D. Jewitt, and K. Keil (Univ. of Arizona, Tucson 2007) p. 297
81. J. Heyvaerts, C. Norman: ApJ **347**, 1055 (1989)
82. S. Hirose, Y. Uchida, K. Shibata, R. Matsumoto: PASJ **49**, 193 (1997)
83. D. Hollenbach, D. Johnstone, S. Lizano, F. Shu: ApJ **428**, 654 (1994)
84. C. Hunter: ApJ **218**, 834 (1977)
85. L. Jin: ApJ **457**, 798 (1996)
86. C. M. Johns-Krull, T. P. Greene, G. W. Doppmann, K. R. Covey: ApJ **700**, 1440 (2009)
87. B. D. Kane, D. P. Clemens: AJ **113**, 1799 (1997)
88. J. F. Kartje: ApJ **452**, 565 (1995)
89. L. Kirby: ApJ **694**, 1056 (2009)
90. A. Königl: ApJ **342**, 208 (1989)
91. A. Königl: ApJ **370**, L39 (1991)
92. A. Königl: LNP **465**, 282 (1996)
93. A. Königl: ApJ **617**, 1267 (2004)
94. A. Königl, J. F. Kartje: ApJ **434**, 446 (1994)
95. A. Königl, R. E. Pudritz: Disk Winds and the Accretion-Outflow Connection. In: *Protostars and Planets IV*, ed by V. Mannings, A. P. Boss, S. S. Russell (Univ. of Arizona, Tucson 2000) p. 759
96. A. Königl, S. P. Ruden: Origin of outflows and winds. In: *Protostars and Planets III*, ed by E. H. Levy, J. I. Lunine (Univ. of Arizona, Tucson 1993) p. 641

97. A. Königl, R. Salmeron, M. Wardle: MNRAS **401**, 479 (2010)
98. A. Königl, M. Wardle: MNRAS **279**, L61 (1996)
99. R. Krasnopolsky, A. Königl: ApJ **580**, 987 (2002)
100. A. K. Kulkarni, M. M. Romanova: MNRAS **398**, 701 (2009)
101. M. W. Kunz, S. A. Balbus: MNRAS **348**, 355 (2004)
102. R. Kurosawa, T. J. Harries, N. H. Symington: MNRAS **370**, 580 (2006)
103. T. Kuwabara, K. Shibata, T. Kudoh, R. Matsumoto: ApJ **621**, 921 (2005)
104. L. D. Landau, E. M. Lifshitz: *Fluid Mechanics*, 2nd edn (Butterworth-Heinemann, Oxford 1987)
105. R. B. Larson: MNRAS **145**, 271 (1969)
106. A. Lazarian: JQSRT **106**, 225 (2007)
107. G. Lesur, P.-Y. Longaretti: A&A **504**, 309 (2009)
108. A. Levinson: ApJ **648**, 510 (2006)
109. E. H. Levy, C. P. Sonett: Meteorite Magnetism and Early Solar System Magnetic Fields. In: *Protostars and Planets*, ed by T. Gehrels (Univ. of Arizona, Tucson 1978) p. 516
110. Z.-Y. Li: ApJ **465**, 855 (1996a)
111. Z.-Y. Li: ApJ **473**, 873 (1996b)
112. Z.-Y. Li, C. F. McKee: ApJ **464**, 373 (1996)
113. Z.-Y. Li, F. H. Shu: ApJ **475**, 237 (1997)
114. D. N. C. Lin, J. E. Pringle: MNRAS **225**, 607 (1987)
115. L. Loinard, A. J. Mioduszewski, L. F. Rodríguez, R. A. González, M. I. Rodríguez, R. M. Torres: ApJ **619**, 179 (2005)
116. M. Long, M. M. Romanova, R. V. E. Lovelace: ApJ **634**, 1214 (2005)
117. M. Long, M. M. Romanova, R. V. E. Lovelace: MNRAS **374**, 436 (2007)
118. M. Long, M. M. Romanova, R. V. E. Lovelace: MNRAS **386**, 1274 (2008)
119. R. V. E. Lovelace, M. M. Romanova, G. S. Bisnovatyi-Kogan: MNRAS **275**, 244 (1995)
120. S. H. Lubow, J. C. B. Papaloizou, J. E. Pringle: MNRAS **267**, 235 (1994a)
121. S. H. Lubow, J. C. B. Papaloizou, J. E. Pringle: MNRAS **268**, 1010 (1994b)
122. D. Lynden-Bell, C. Boily: MNRAS **267**, 146 (1994)
123. M. N. Machida, S. Inutsuka, T. Matsumoto: ApJ **670**, 1198 (2007)
124. M. N. Machida, T. Matsumoto, T. Hanawa, K. Tomisaka: ApJ **645**, 1227 (2006)
- bibitemjournal M.-M. Mac Low, M. L. Norman, A. Königl, M. Wardle: ApJ **442**, 726 (1995)
125. S. C. Martin: ApJ **473**, 1051 (1996)
126. S. Matt, R. E. Pudritz: ApJ **607**, L43 (2004)
127. S. Matt, R. E. Pudritz: MNRAS **356**, 167 (2005)
128. S. Matt, R. E. Pudritz: ApJ **681**, 391 (2008)
129. Z. Meliani, F. Casse, C. Sauty: A&A **460**, 1 (2006)
130. R. Mellon, Z.-Y. Li: ApJ, **698**, 922 (2009)
131. F. Ménard, G. Duchêne: A&A **425**, 973 (2004)
132. R. Millan-Gabet, F. Malbet, R. Akeson, C. Leinert, J. Monnier, R. Waters: The Circumstellar Environments of Young Stars at AU Scales. In: *Protostars and Planets V*, ed by B. Reipurth, D. Jewitt, and K. Keil (Univ. of Arizona, Tucson 2007) p. 539
133. K. A. Miller, J. M. Stone: ApJ **534**, 398 (2000)
134. M. Mitchner, C. H. Jr. Kruger: *Partially Ionized Gases*, (Wiley, New York 1973)

135. S. Mohanty, R. Jayawardhana, G. Basri: ApJ **626**, 498 (2005)
136. T. Ch. Mouschovias: ApJ **207**, 141 (1976)
137. T. Ch. Mouschovias, K. Tassis, M. W. Kunz: ApJ **646**, 1043 (2006)
138. T. Muto, M. N. Machida, S. Inutsuka: ApJ **679**, 813 (2008)
139. J. R. Najita, J. S. Carr, A. E. Glassgold, J. A. Valenti: Gaseous Inner Disks. In: *Protostars and Planets V*, ed by B. Reipurth, D. Jewitt, and K. Keil (Univ. of Arizona, Tucson 2007) p. 507
140. F. Nakamura, T. Hanawa, T. Nakano: ApJ **444**, 770 (1995)
141. T. Nakano, R. Nishi, T. Umebayashi: ApJ **573**, 199 (2002)
142. A. Natta, L. Testi, N. Calvet, Th. Henning, R. Waters, D. Wilner: Dust in Protoplanetary Disks: Properties and Evolution. In: *Protostars and Planets V*, ed by B. Reipurth, D. Jewitt, and K. Keil (Univ. of Arizona, Tucson 2007) p. 767
143. D. A. Neufeld, D. J. Hollenbach: ApJ **428**, 170 (1994)
144. R. Nishi, T. Nakano, T. Umebayashi: ApJ **368**, 181 (1991)
145. H. Nomura, Y. Nakagawa: ApJ **640**, 1099 (2006)
146. D. O'Brien, P. Garcia, J. Ferreira, S. Cabrit, L. Binette: Ap&SS **287**, 129 (2003)
147. G. I. Ogilvie: MNRAS **288**, 63 (1997)
148. G. I. Ogilvie, M. Livio: ApJ **553**, 158 (2001)
149. N. Ohashi, M. Hayashi, P. T. P. Ho, M. Momose: ApJ **475**, 211 (1997)
150. I. Okamoto: MNRAS **173**, 357 (1975)
151. M. Oppenheimer, A. Dalgarno: ApJ **192**, 29 (1974)
152. E. N. Parker: *Cosmical Magnetic Fields: Their Origin and Their Activity*, (Clarendon, Oxford 1979)
153. E. N. Parker: *Conversations on Electric and Magnetic Fields in the Cosmos*, (Princeton Univ., Princeton 2007)
154. G. Pelletier, R. E. Pudritz: ApJ **394**, 117 (1992)
155. M. V. Penston: MNRAS **144**, 425 (1969)
156. N. Pesenti, C. Dougados, S. Cabrit, J. Ferreira, F. Casse, P. Garcia, D. O'Brien: A&A **416**, L9 (2004)
157. L. Podio, F. Bacciotti, B. Nisini, J. Eislöffel, F. Massi, T. Giannini, T. P. Ray: A&A **456**, 189 (2006)
158. R. E. Pudritz, R. Ouyed, Ch. Fendt, A. Brandenburg: Disk Winds, Jets, and Outflows: Theoretical and Computational Foundations. In: *Protostars and Planets V*, ed by B. Reipurth, D. Jewitt, and K. Keil (Univ. of Arizona, Tucson 2007) p. 277
159. T. Ray, C. Dougados, F. Bacciotti, J. Eislöffel, A. Chrysostomou: Toward Resolving the Outflow Engine: An Observational Perspective. In: *Protostars and Planets V*, ed by B. Reipurth, D. Jewitt, and K. Keil (Univ. of Arizona, Tucson 2007) p. 231
160. T. P. Ray, T. W. B. Muxlow, D. J. Axon, A. Brown, D. Corcoran, J. Dyson, R. Mundt: Nature **385**, 415 (1997) A. Shukurov: A&A **398**, 825 (2003)
161. J. Richer, D. Shepherd, S. Cabrit, R. Bachiller, E. Churchwell: Molecular Outflows from Young Stellar Objects. In: *Protostars and Planets IV*, ed by V. Mannings, A. P. Boss, S. S. Russell (Univ. of Arizona, Tucson 2000) p. 867
162. M. M. Romanova, A. K. Kulkarni, R. V. E. Lovelace: ApJ **673**, L171 (2008)
163. M. M. Romanova, G. V. Ustyugova, A. V. Koldoba, R. V. E. Lovelace: ApJ **578**, 420 (2002)

164. M. M. Romanova, G. V. Ustyugova, A. V. Koldoba, R. V. E. Lovelace: ApJ **610**, 920 (2004)
165. M. M. Romanova, G. V. Ustyugova, A. V. Koldoba, R. V. E. Lovelace: ApJ **635**, L165 (2005)
166. M. M. Romanova, G. V. Ustyugova, A. V. Koldoba, R. V. E. Lovelace: MNRAS **399**, 1802 (2009)
167. M. M. Romanova, G. V. Ustyugova, A. V. Koldoba, J. V. Wick, R. V. E. Lovelace: ApJ **595**, 1009 (2003)
168. D. M. Rothstein, R. V. E. Lovelace: ApJ **677**, 1221 (2008)
169. P. N. Safier: ApJ **408**, 115 (1993a)
170. P. N. Safier: ApJ **408**, 148 (1993b)
171. T. Sakurai: A&A **152**, 121 (1985)
172. R. Salmeron, A. Königl, M. Wardle: MNRAS **375**, 177 (2007)
173. R. Salmeron, A. Königl, M. Wardle: MNRAS (to be submitted 2010)
174. T. Sano, S. M. Miyama, T. Umebayashi, T. Nakano: ApJ **543**, 486 (2000)
175. T. Sano, J. M. Stone: ApJ **577**, 534 (2002)
176. D. A. Schleuning: ApJ **493**, 811 (1998)
177. H. Shang, A. E. Glassgold, F. H. Shu, S. Lizano: ApJ **564**, 853 (2002)
178. H. Shang, S. Lizano, A. E. Glassgold, F. H. Shu: ApJ **612**, L69 (2004)
179. D. Shepherd: Massive Molecular Outflows. In: *Massive Star Birth: A Crossroads of Astrophysics*, ed by R. Cesaroni et al. (Cambridge Univ., Cambridge 2005) p. 237
180. F. H. Shu: ApJ **214**, 488 (1977)
181. F. H. Shu, F. C. Adams, S. Lizano: ARA&A **25**, 23 (1987)
182. F. H. Shu, D. Galli, S. Lizano, C. Mike: ApJ **647**, 382 (2006)
183. F. H. Shu, S. Lizano, D. Galli, M. J. Cai, S. Mohanty: ApJ **682**, L121 (2008)
184. F. H. Shu, J. R. Najita, E. C. Ostriker, H. Shang: ApJ **455**, L155 (1995)
185. F. H. Shu, J. R. Najita, H. Shang, Z.-Y. Li: X-Winds Theory and Observations. In: *Protostars and Planets IV*, ed by V. Mannings, A. P. Boss, S. S. Russell (Univ. of Arizona, Tucson 2000) p. 789
186. N. Soker: A&A **435**, 125 (2005)
187. N. Soker, O. Regev: ApJ **406**, 603 (2003)
188. H. C. Spruit: Magnetohydrodynamic Jets and Winds from Accretion Disks. In: *Evolutionary processes in Binary Stars*, NATO ASIC Proc. **477**, 249 (1996)
189. H. C. Spruit, R. Stehle, J. C. B. Papaloizou: ApJ **275**, 1223 (1995)
190. H. C. Spruit, D. A. Uzdensky: ApJ **629**, 960 (2005)
191. K. G. Stassun, R. D. Mathieu, T. Mazeh, F. J. Vrba: AJ **117**, 2941 (1999)
192. K. G. Stassun, R. D. Mathieu, F. J. Vrba, T. Mazeh, A. Henden: AJ **121**, 1003 (2001)
193. T. Takeuchi, D. N. C. Lin: ApJ **581**, 1344 (2002)
194. L. V. Tambovtseva, V. P. Grinin: AstL **34**, 231 (2008)
195. K. Tassis: MNRAS **379**, L50 (2007)
196. K. Tassis, Ch. Mouschovias: ApJ **618**, 783 (2005)
197. K. Tassis, Ch. Mouschovias: ApJ **660**, 388 (2007)
198. S. A. Teitler: preprint (to be submitted 2010)
199. C. E. J. M. L. J. Terquem: MNRAS **341**, 1157 (2003)
200. I. Tilling, C. J. Clarke, J. E. Pringle, C. A. Tout: MNRAS **385**, 1530 (2008)
201. K. Tomisaka: PASJ **48**, 701 (1996)
202. A. Toomre: ApJ **138**, 385 (1963)

203. M. V. Torbett: ApJ **278**, 318 (1984)
204. C. A. Tout, J. E. Pringle: MNRAS **281**, 219 (1996)
205. K. Tsinganos, C. Sauty, G. Surlantzis, E. Trussoni, J. Contopoulos: MNRAS **283**, 811 (1996)
206. T. Tsuribe: ApJ **527**, 102 (1999)
207. N. J. Turner, T. Sano, N. Dziourkevitch: ApJ **659**, 729 (2007)
208. T. Umebayashi, T. Nakano: MNRAS **218**, 663 (1986)
209. G. V. Ustyugova, A. V. Koldoba, M. M. Romanova, R. V. E. Lovelace: ApJ **646**, 304 (2006)
210. D. Uzdensky, J. Goodman: ApJ **682**, 608 (2008)
211. D. Uzdensky, A. Königl, C. Litwin: ApJ **565**, 1191 (2002a)
212. D. Uzdensky, A. Königl, C. Litwin: ApJ **565**, 1205 (2002b)
213. J. S. Vink, J. E. Drew, T. J. Harries, R. D. Oudmaijer, Y. Unruh: MNRAS **359**, 1049 (2005)
214. N. Vlahakis, K. Tsinganos, C. Sauty, E. Trussoni: MNRAS **318**, 417 (2000)
215. B. von Rekowski, A. Brandenburg: A&A **420**, 17 (2004)
216. B. von Rekowski, A. Brandenburg: AN **327**, 53 (2006)
217. B. von Rekowski, A. Brandenburg, W. Dobler, A. Shukurov: A&A **398**, 825 (2003)
218. B. von Rekowski, N. Piskunov: AN **327**, 340 (2006)
219. E. I. Vorobyov, S. Basu: MNRAS **381**, 1009 (2007)
220. D. Ward-Thompson, P. André, R. Crutcher, D. Johnstone, T. Onishi, C. Wilson: An Observational Perspective of Low-Mass Dense Cores II: Evolution Toward the Initial Mass Function. In: *Protostars and Planets V*, ed by B. Reipurth, D. Jewitt, and K. Keil (Univ. of Arizona, Tucson 2007) p. 33
221. M. Wardle: ASPC **121**, 561 (1997)
222. M. Wardle: MNRAS **307**, 849 (1999)
223. M. Wardle: Ap&SS **311**, 35 (2007)
224. M. Wardle, A. Königl: ApJ **410**, 218 (1993)
225. M. Wardle, C. Ng: MNRAS **303**, 239 (1999)
226. A. M. Watson, K. R. Stpelfeldt, K. Wood, F. Ménard: Multiwavelength Imaging of Young Stellar Object Disks: Toward an Understanding of Disk Structure and Dust Evolution. In: *Protostars and Planets V*, ed by B. Reipurth, D. Jewitt, and K. Keil (Univ. of Arizona, Tucson 2007) p. 523
227. S. J. Weidenschilling: Ap&SS **51**, 153 (1977)
228. C. Zanni, A. Ferrari, R. Rosner, G. Bodo, S. Massaglia: A&A **469**, 811 (2007)
229. E. G. Zweibel, K. T. Hole, R. D. Mathieu: ApJ **649**, 879 (2006)